LIGO-P1900097
INT-PUB-19-009

Constraining the neutron-matter equation of state with gravitational waves

Michael McNeil Forbes,[1,2,*] Sukanta Bose,[1,3,†] Sanjay Reddy,[4,‡]
Dake Zhou,[2,§] Arunava Mukherjee,[5,6,¶] and Soumi De[7,**]

[1]*Department of Physics & Astronomy, Washington State University, Pullman, Washington 99164–2814,* USA
[2]*Department of Physics, University of Washington, Seattle, Washington 98195–1560,* USA
[3]*Inter-University Centre for Astronomy and Astrophysics, Post Bag 4, Ganeshkhind, Pune 411 007, India*
[4]*Institute for Nuclear Theory, University of Washington, Seattle, Washington 98195–1560,* USA
[5]*Max-Planck-Institut für Gravitationsphysik (Albert Einstein Institute), D-30167 Hannover, Germany*
[6]*Leibniz Universität Hannover, D-30167 Hannover, Germany*
[7]*Department of Physics, Syracuse University, Syracuse, New York 13244,* USA

We show how observations of gravitational waves from binary neutron star (BNS) mergers over the next few years can be combined with insights from nuclear physics to obtain useful constraints on the equation of state (EOS) of dense matter, in particular, constraining the neutron-matter EOS to within 20% between one and two times the nuclear saturation density $n_0 \approx 0.16\,\mathrm{fm}^{-3}$. Using Fisher information methods, we combine observational constraints from simulated BNS merger events drawn from various population models with independent measurements of the neutron star radii expected from x-ray astronomy (the Neutron Star Interior Composition Explorer (NICER) observations in particular) to directly constrain nuclear physics parameters. To parameterize the nuclear EOS, we use a different approach, expanding from pure nuclear matter rather than from symmetric nuclear matter to make use of recent quantum Monte Carlo (QMC) calculations. This method eschews the need to invoke the so-called parabolic approximation to extrapolate from symmetric nuclear matter, allowing us to directly constrain the neutron-matter EOS. Using a principal component analysis, we identify the combination of parameters most tightly constrained by observational data. We discuss sensitivity to various effects such as different component masses through population-model sensitivity, phase transitions in the core EOS, and large deviations from the central parameter values.

CONTENTS

* mforbes@alum.mit.edu
† sukanta@wsu.edu
‡ sareddy@uw.edu
§ zdk@uw.edu
¶ arunava.mukherjee@aei.mpg.de
** sde101@syr.edu

I. INTRODUCTION

The detection of gravitational waves from the binary neutron star (BNS) merger GW170817 by the advanced laser interferometer gravitational wave observatory (aLIGO) detectors [1] in Hanford, WA (LHO) and Livingston, LA (LLO) and the VIRGO detector [2] ushered in the era of multi-messenger astronomy with gravitational waves [3, 4]. This has been instrumental in launching novel ways of constraining cosmological parameters [5–8], on the one hand, and neutron star equation of state (EOS) parameters, on the other hand [3, 9]. In a BNS system the neutron star masses and their EOS determine how much quadrupolar deformation $\mathcal{Q}_{ij}$ their tidal fields $\mathcal{E}_{ij}$ are able to induce in each other. The two are related by the tidal deformability parameter λ as $\mathcal{Q}_{ij} = -\lambda\mathcal{E}_{ij}$. It is now well understood that the tidal deformability parameters of both neutron stars in a double neutron star system affect the phase of the gravitational wave signal during the late stages of the inspiral [10].

Recent articles that followed discovery of GW170817 have shown that upper bounds on the dimensionless tidal deformability $\Lambda = \lambda c^{10}/(GM)^5$ of the neutron stars obtained from gravitational wave data analysis provide constraints on the EOS of dense matter encountered inside neutron stars [11–13]. This is a great opportunity and challenge for several reasons: neutron rich matter, although relevant for many applications, is not easily accessible in experiments, while theoretical approaches require solving the difficult quantum many-body problem and lack a precise characterization of the underlying interactions. Observational constraints provide an anchor for nuclear theory in this uncertain regime, allowing one to extrapolate low-density and symmetric properties of nuclear matter to significantly improve constraints on neutron-rich matter at higher densities.

In this article we discuss how we can extract more detailed information about the properties of dense neutron-rich matter and neutron stars during the next few years with more gravitational wave detections and measurements of neutron star radii expected from x-ray astronomy, and highlight the importance of an informed parameterization of the dense matter EOS. We make the reasonable assumption that all neutron stars are described by the same EOS. Further, modern nuclear Hamiltonians based on chiral effective field theory provide a systematic momentum expansion of two- and many-body nuclear forces. This, combined with advanced computational methods to solve the non-relativistic quantum many-body problem, now allows us to calculate the EOS of pure neutron matter up to nucleon number density $n_c \approx 2n_0$, where $n_0 = 0.16$ nucleons per fm^3 is the average nucleon density inside large nuclei (corresponding to a mass density $\rho_0 \simeq 2.7 \times 10^{14}\,\mathrm{g/cm^3}$) [14]. Interestingly, there is a convergence of different ab initio methods based on realistic microscopic Hamiltonians that account for two and three neutron forces [15]. These calculations suggest that the functional form of the EOS of pure neutron in the density interval $0.5n_0$ to $2n_0$ is well determined. We use this information to parameterize the EOS and show how it helps with the analysis of multiple BNS detections and provide tighter and more useful constraints for dense matter physics. In turn, these constraints for the EOS of pure neutron in the density interval where calculations are feasible will provide new insights for nuclear physics.

Our study differs from earlier work in the following aspects:

- We incorporate insights about neutron-rich matter obtained from nuclear physics by implementing a new parameterization of nuclear equation of state and identify parameters that can be best constrained by gravitational wave observations.
- We quantify how constraints on these parameters and on the pressure of neutron matter in the density interval n_0 to $2n_0$ will improve with the number of detections.
- Our analysis uses a numerical relativity based tidal waveform model.
- We study the effect of different population synthesis models on the accuracy with which EOS parameters can be measured with gravitational waves and use several thousand binary neutron star source simulations to assess errors in EOS parameter measurements.
- While a nearby event like GW170817 at aLIGO design sensitivity would significantly constrain the properties of neutron matter, we show that similar constraints can be obtained from about 15 events beyond 100 Mpc.

We begin with a summary of our results in section II, then describe how we have parameterized the dense matter EOS in section III. In section IV we discuss how we obtain constraints from the gravitational waveform of simulated merger events. Finally, we discuss details of the method we use to obtain these constrains in section VI.

II. RESULTS

Our main result is that even a handful of gravitational wave observations of BNS mergers will provide the most stringent constraints on the low-temperature equation of state of dense neutron matter in the density interval between $n_0 - 2n_0$. This is summarized in Fig. 1, which shows how the constraints on the pressure of pure neutron matter $P_n(n_n)$ improve as a function of additional NICER or LIGO observations. We start from the errors listed in Table I, which, for the purposes of this analysis, we interpret as uncorrelated 1σ normal errors for the parameters. This gives the upper dotted line labeled "Nuclear".

To this, we add the following constraints:

- Constraints from a simulated binary with similar masses and distance $D \sim 40$ Mpc to GW170817 but at aLIGO design sensitivity.
- Gravitational wave observations at aLIGO design sensitivity of $N_{obs} \in \{1, 15, 100\}$ distant $D \in [100, 400]$ Mpc simulated merger events from population model `SubSolarA` as described in section IV. To estimate the variance possible within the population model, we sample 500 different populations, each containing N_{obs}, and plot the 1σ (68th percentile) error bands as shaded regions.
- An uncorrelated mass and radius measurement of J0437 projected to be measured at a 5% level

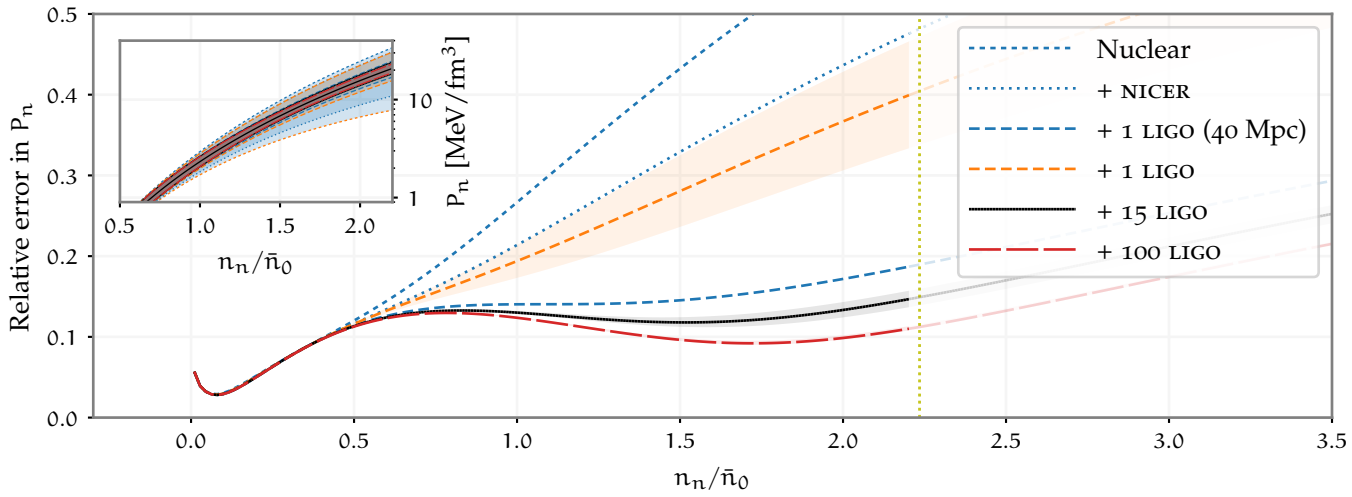

Figure 1. (color online) Relative constraints on the pressure of neutron matter $P_n(n_n)$ from $N_{obs} \in \{1, 15, 100\}$ simulated merger events, and expected constraints from NICER (J0437) [16] ($M = 1.44(7)M_\odot$, $\delta R/R = 0.1$). From top: constraints from nuclear theory augmented by NICER, from a single merger event at $D = 40$ Mpc with aLIGO sensitivity, then various N_{obs} LIGO events drawn from `SubSolarA` that have $D \in [100, 400]$Mpc. The shading shows the range of sampling errors (1σ or 68th percentile) demonstrating variation within the `SubSolarA` population model [17]. Beyond the vertical yellow line, we use the core equation of state (EOS). Inset: $P_n(n_n)$ with 1σ error bands corresponding to each of the constraints.

from NASA's NICER mission – i.e. $1.44(7)M_\odot$ with a 10% measurement of R [16, 18].

This analysis demonstrates several key points: A nearby event such as GW170817 is comparable to a dozen or so events from $D \geqslant 100$ Mpc. The NICER constraints are comparable to a single LIGO observation from a distant population sample having low signal-to-noise ratio (SNR), however, nearby or multiple accumulated LIGO events yield significant improvement. After about $N_{obs} = 15$ observation, we observe rather limited improvement from additional $N_{obs} = 100$. This can also be seen in Fig. 2, which shows how the constraints improve as a function of the number of observations.

One caveat: these constraints assume Gaussian errors and linear error propagation. A proper analysis requires a much more expensive Bayesian approach (see, e.g., Ref. [19]). To assess the non-linear effects, we provide similar plots for comparison in [20] for the different central values listed in Table II.

To put these results in perspective, consider the nuclear symmetry energy S_{sym} and the slope of its density dependence L,

$$S_{sym} = E_{np}(n_0, 0) - E_{np}(\tfrac{n_0}{2}, \tfrac{n_0}{2}), \tag{1a}$$

$$L = 3n_0 \left.\frac{\partial E_{np}(n_n, 0)}{\partial n_n}\right|_{n_n = n_0} = 3\frac{P_n(n_0)}{n_0}, \tag{1b}$$

where $E_{np}(n_n, n_p)$ is the energy-per-particle of uniform nuclear matter. If the so-called parabolic approximation holds at saturation ($L_2 \approx L$ – see Eq. (5) and the surrounding discussion), then upcoming neutron skin experiments [21] expect to constrain $\Delta L = 41$ MeV with a possible reduction to $\Delta L = 15$ MeV with a followup experiment. This is comparable to combined constraints from ab initio calculations [22–25] and astrophysical observations [15, 26–28]. From our analysis we thus see that gravitational wave observations alone could have an impact at the ~ 15% level corresponding to $\Delta L \approx 10$ MeV.

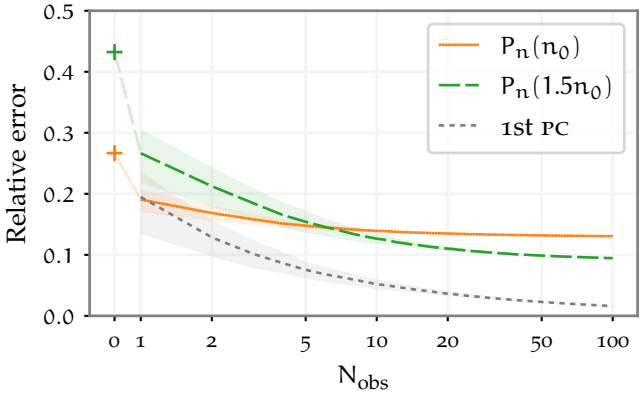

Figure 2. (color online) Improvement in relative constraint on the pressure of neutron matter $P_n(n_n)$ at $n_n = 1.5n_0$ and $n_n = n_0$ (related to the slope $L = 3P_n(n_0)/n_0$ of the symmetry energy) to an increasing number of simulated merger events applied to the initial nuclear constraints denoted with a plus at $N_{obs} = 0$. The shading shows the range of sampling errors (1σ or 68th percentile) demonstrating variation within the `SubSolarA` population model. The lower dotted curve shows the level of the most tightly constrained principal component (1st PC).

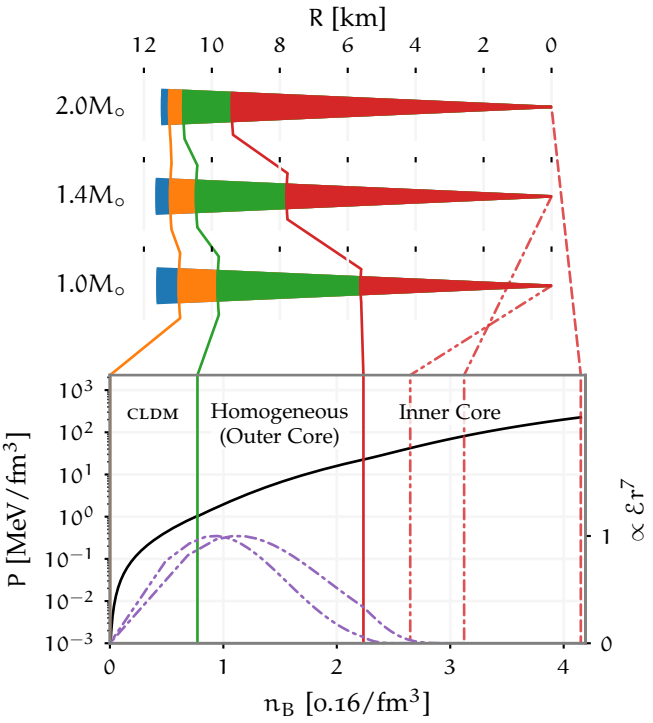

Figure 3. (color online) Regions of the neutron star. The upper three wedges represent a cross-section of $M = 2M_\odot$, $M = 1.4M_\odot$, and $M = 1M_\odot$ neutron stars respectively. As discussed in the text, the unified EOS smoothly connects four distinct regions from low density on the left to high density on the right. The radius of these transitions for the `Central` parameter values is shown in the top plot. These are connected to the equation of state expressed in terms of the pressure $P(n_B)$ (solid (black) line on left axis) as a function of the total baryon density in units of the saturation density $n_0 = 0.16\,\mathrm{fm}^{-3}$. From low to high density, the regions of the EOS are: a) the outer crust (very low density which is too small to see on the lower plot) that interpolates the data of [29] and [30] as tabulated in [31] (blue) with minor corrections to ensure convexity as discussed in [20]; b) the inner crust modeled by the CLDM [32] (orange); c) the outer core of homogeneous nuclear matter in beta-equilibrium (green); d) the inner core equation of state parameterized by a quadratic speed of sound (red). At the right, the various (red) dashed lines correspond to the core density of the respective stars. At the bottom are corresponding dashed curves (purple) proportional to $\mathcal{E}r^7$ (normalized to the maximum value on the right axis) for the two lower-mass stars. This roughly correlates with the local contribution to the dimensionless tidal deformability [33].

III. PARAMETERIZATION OF THE NUCLEAR EQUATION OF STATE

To relate the nuclear equation of state to the structure of neutron stars, we must first characterized the equation of state (EOS) of nuclear matter. This is conveniently parameterized by the energy density $\mathcal{E}(n_B)$ as a function of the baryon number density $n_B = n_n + n_p$, which is the sum of the neutron and proton number densities. Simple approximation for this function in terms of polytropes are often a starting point for astrophysical analysis. Indeed, many families of nuclear EOS can be characterized quite well by a simple set of piecewise polytropes [34].

Our approach here, however, is to directly express $\mathcal{E}(n_B)$ in terms of nuclear physics parameters. This approach allows one to directly assess how observations translate into constraints on nuclear physics. We shall demonstrate this by providing constraints on the pressure of pure neutron matter $P_n(n_n)$, which is inaccessible from a general polytropic analysis (Fig. 1).

It is useful to divide the neutron star interior into four regions: the outer crust, the inner crust, the outer core, and the inner core. The radial extent of the outer crust, which is composed neutron-rich nuclei embedded in a electron gas, is only a few hundred meters and its contribution to the neutron star mass is negligible. The EOS of the outer crust is well understood and depends weakly on the composition of nuclei present. The inner crust extends from $n = n_{drip} \simeq 2\times10^{-3}n_0$ to $n = n_{core} \simeq 2n_0$, has radial thickness $\sim$ 512km, and contains a modest fraction of the mass. Here, exotic neutron-rich nuclei are embedded in a dense liquid of neutrons and electrons, as described by the compressible liquid-drop model (CLDM) in section III A. The outer core is a liquid composed primarily of neutrons and a small (few percent) admixture of protons, electrons, and muons. It extends from $n \sim 0.5n_0$ to $n = n_c \sim 2n_0$ where the description of matter in terms of nucleons interacting with static potentials is expected to break down. The inner core extends to higher densities, and we switch here to the speed-of-sound parameterization discussed in section III C.

On dimensional grounds one expects the dimensionless tidal deformability Λ to be related to $\int_0^R \mathcal{E}r^n dr = \langle \mathcal{E}r^n \rangle$ with $n \sim 7$ for $M \sim 1.4M_\odot$ [33]. Although the EOS around intermediate densities dominates the 7th moment of energy distribution for massive neutron stars, the inner crust also makes a large contribution to Λ for low-mass stars (which are believed to be more common in binary neutron star systems). This contribution is shown by the dashed (purple) lines at the bottom of Fig. 3. Thus, it is important to provide a unified description of the EOS of the inner crust and the outer core in any analysis that aims to constrain the EOS using gravitational wave observations of binary neutron stars.

A. Compressible Liquid Drop Model

The compressible liquid-drop model (CLDM) (see [32]) provides a unified EOS connecting a fixed outer crust for $\rho < \rho_{drip}$ (for which we use the data in Table 4 of [31]) to the inner core EOS. In the inner crust, the CLDM constructs spherical nuclei in a spherical Wigner-

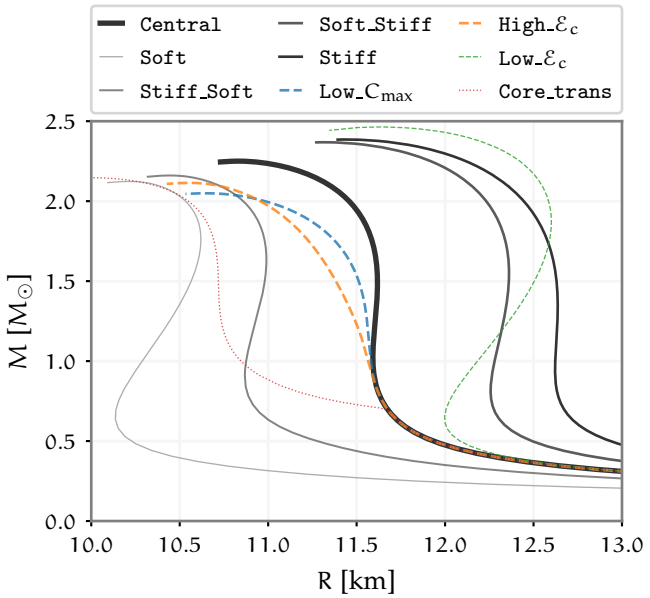

Figure 4. (color online) Mass-radius curves for the EOSs considered in Table II. The thick solid curve is our `Central` EOS. Dashed curves correspond to different core parameterizations. Thin curves correspond to EOSs for which astrophysical observations would provide poor constraints for nuclear physics. These include a sharp first-order transition in the core (`Core_trans`), and soft EOSs (`Soft` and `Stiff_Soft`) which form very compact objects with low deformability. The `Low_`$\mathcal{E}_c$ EOS also poorly constrains nuclear physics since the core appears close to the saturation density. As shown later in Fig. 9, for these types of EOS, observations constrain the core parameters rather than the properties of neutron matter.

Seitz cell, ensuring equilibrium with surrounding neutron and lepton gases by establishing both electric and β-equilibrium. This is similar to the approach taken in [35, 36], but differs in how we define the nuclear matter EOS $\mathcal{E}_{np}(n_n, n_p)$. Instead of using $\mathcal{E}_{np}(n_n, n_p)$ obtained from specific models based on effective Hamiltonians solved in the mean field approximation to reproduce empirical parameters like nuclear saturation properties, we use what we believe is close to a minimal phenomenological parameterization that directly encodes properties that can either be measured or calculated reliably. The advantage of our approach is that these parameters are directly connected with the unified EOS, allowing us to provide a full covariance analysis linking nuclear parameters with neutron star observables.

Although the use of a spherical Wigner-Seitz cell precludes the possibility of pasta phases [37] the errors incurred by the Wigner-Seitz approximation for different lattice structures are less then 0.5% (see e.g. [32, 38]).

Our implementation of the CLDM introduces two effective parameters: the surface tension σ_0 and the parameter $C_{sym} = \sigma_\delta/\sigma_0$ which characterizes the isospin dependence of the surface tension $\sigma(n_n, n_p) = \sigma_0(1 - C_{sym}(\beta_p)^2 + \mathcal{O}(\beta_p^4))$ [39] (see [20] for the exact form used), where $\beta_p = (n_n - n_p)/(n_n + n_p)$ is the isospin asymmetry. We fix the parameter σ_0 to smoothly match the tabulated outer crust equation of state, leaving free the single parameter σ_δ. Additionally, we include as a parameter a suppression factor $\mathcal{C}$ for the Coulomb interaction to allow for the diffusivity of the proton charge distribution (see the discussion in [40]). As will be shown in section II, these parameters have negligible effects on the constructed equation of state (EOS).

This approach allows for a small first-order phase transition from the region modeled by the CLDM to homogeneous nuclear matter. With our parameters, this phase transition is weak: $\delta n < 0.002\,\mathrm{fm}^{-3}$.

To establish β-equilibrium we include leptons modeled as a Fermi gas of electrons (and muons at sufficiently high densities) in the Thomas-Fermi (TF) approximation.

B. Homogeneous Nuclear Matter

One of the main new features of our analysis is to parameterize the nuclear-matter EOS as an expansion in the proton fraction $x_p = n_p/(n_n + n_p)$ from pure neutron matter to symmetric neutron matter. This is in contrast to the common approach of expanding about symmetric nuclear matter in powers of the isospin asymmetry $\beta_p = (n_n - n_p)/(n_n + n_p)$. The common approach allows one to directly connect experimentally relevant properties of symmetric nuclear matter to properties of neutron matter. This connection, however, is generally predicated on the so-called parabolic approximation, which is valid only if quadratic terms β_p^2 dominate over quartic β_p^4 and higher-order terms. While there is some support for this below saturation density from relativistic Dirac-Bruckner-Hartree-Fock (DBHF) calculations [45], Gogny forces [46], and other perturbative techniques (see [47] for a review), it is not well established at higher densities. Indeed virtually any form of neutron-matter EOS can be accommodated with quartic β_p^4 terms without spoiling global mass fits [48]. For this reason, we start with a parameterization of pure neutron matter, then use the properties of symmetric nuclear matter to constrain the extrapolation in the proton fraction x_p.

To describe pure neutron matter we use a double polytrope for the energy per particle:

$$E_n(n_n) = \frac{\mathcal{E}_n(n_n)}{n_n} = m_N c^2 + a\left(\frac{n_n}{\bar{n}_0}\right)^\alpha + b\left(\frac{n_n}{\bar{n}_0}\right)^\beta,$$
$$P_n = n_n\left[a\alpha\left(\frac{n_n}{\bar{n}_0}\right)^\alpha + b\beta\left(\frac{n_n}{\bar{n}_0}\right)^\beta\right], \qquad (2)$$

where m_N is the nucleon mass, $\bar{n}_0 = 0.16\,\mathrm{fm}^{-3}$ is a constant (approximately the nuclear saturation density),

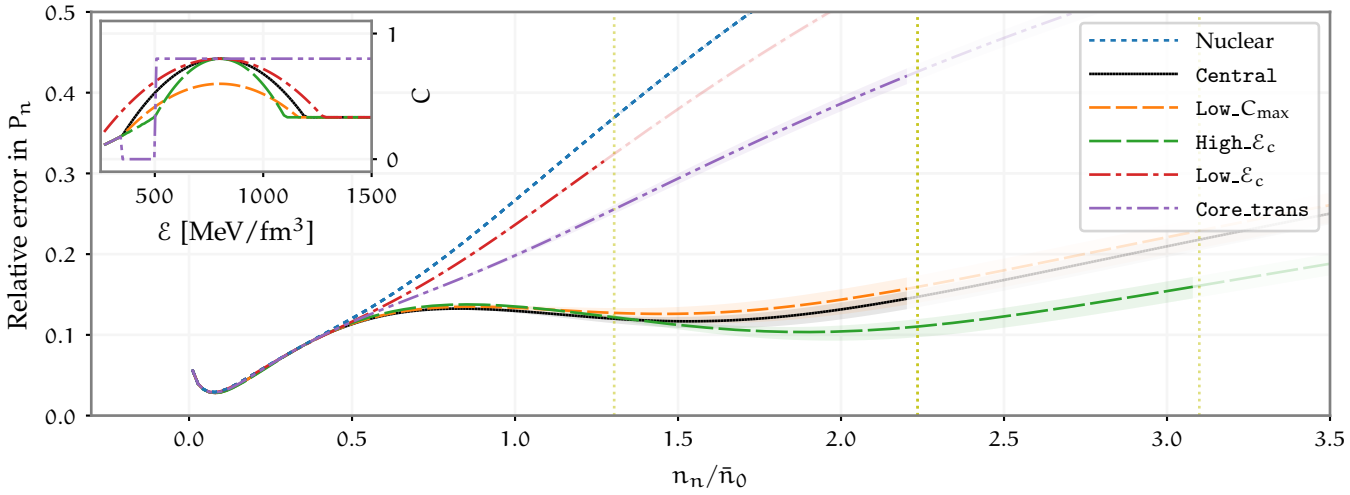

Figure 5. (color online) Sensitivity of the constraint on the pressure of neutron matter $P_n(n_n)$ from $N_{obs} = 15$ simulated merger events drawn from the SubSolarA population model to variations of the core equation of state. The vertical yellow lines denote the density n_c at which the EOS reverts to the core form. Inset: form of the various core speed-of-sound functions $C(\mathcal{E}) = c_s^2/c^2$.

and a, b, α, and β are four EOS parameters. This form was found to accurately fit QMC calculations of the EOS using nuclear Hamiltonians with realistic two- and three-body forces [15], and is consistent with recent QMC results based on chiral EFT interactions [23–25, 42]. For small proton fractions $x_p = n_p/(n_n + n_p)$, we perform an expansion:

$$E_{np}(n_n, n_p) = (1-x_p)E_n(n_n) + x_p\left(m_p c^2 + \Sigma^p(n_B)\right) + \\ + \frac{\hbar^2(3\pi^2)^{2/3}}{2m^*}x_p^{5/3}n_B^{2/3} + x_p^2 f_2(n_B) + x_p^3 f_3(n_B) + \cdots \tag{3}$$

where m^* is the proton effective mass, and $\Sigma^p(n_B)$ describes the self-energy of the proton polaron. This function is presently poorly constrained by QMC and experimental data and all known results are consistent with a simple two-parameter quadratic expansion:

$$\Sigma^p(n_B) = \mu_p \frac{n_B}{\bar{n}_0}\frac{u_p - \frac{n_B}{\bar{n}_0}}{u_p - 1} \tag{4}$$

where $\mu_p = \Sigma^p(\bar{n}_0)$ and $u_p = n_B/\bar{n}_0$ where $\Sigma^p(n_B) = 0$ returns to zero. (We expect $\Sigma^p(n_B)$ to curve up for higher densities due to the repulsive nature of nuclear three-body interactions).

The additional powers $f_n(n_B)$ are chosen to match the properties of nuclear matter to quadratic order in the isospin asymmetry β_p and expansion away from saturation δ_n:

$$E_{np}^{sym}(n_n, n_p) = \varepsilon_0 + \frac{K_0}{2}\delta_n^2 + \left(S_2 + L_2\delta_n + \frac{K_2}{2}\delta_n^2\right)\beta_p^2, \\ \beta_p = \frac{n_n - n_p}{n_B}, \qquad \delta_n = \frac{n_B - n_0}{3n_0}. \tag{5}$$

Fitting two even powers, β_p^0 and β_p^2, and the lack of odd powers uniquely defines the functions $f_2(n_B)$ through $f_5(n_B)$, completing our characterization of the nuclear equation of state in terms of the nuclear saturation density n_0, energy ε_0, and incompressibility K_0; the symmetry energy S_2, slope L_2 and incompressibility K_2. Note that a term proportional to β_p^4 is allowed in Eq. (5), but our EOS is unconstrained by this term, i.e., does not rely on the parabolic approximation Eq. (5).

C. Speed of Sound Parameterization of the Inner Core

Above densities $n_c \sim 2n_0$ the EOS is virtually unconstrained. The typical approximation at high density is in terms of a polytrope, but we choose a more physically motivated high-density EOS parameterized in terms of the square of the speed of sound: $C(\mathcal{E}) = c_s^2(\mathcal{E})/c^2 = P'(\mathcal{E}) \leqslant 1$ which approaches the perturbative quantum chromodynamics (PQCD) result $C(\mathcal{E}) \to 1/3$ at asymptotic densities. Although the form of the function $C(\mathcal{E})$ is unknown at finite density, its qualitative form at finite temperature suggests that it may first peak before returning to the asymptotic value [14, 49]. We thus include a simple parameterization $C(\mathcal{E})$ as a quadratic polynomial smoothly connecting to the homogeneous equation of state at a fixed transition energy density $\mathcal{E}_c$ reaching a maximum $C_{max} \leqslant 1$ at an energy density $\mathcal{E}_{max}$, then returning to $C = 1/3$ at which it remains for higher densities. This core EOS thus introduces three parameters $\mathcal{E}_c$, C_{max}, and $\mathcal{E}_{max}$. To better understand the sensitivity of our results to the properties of the core, we include one slightly different form Core_trans which has a first-order phase transition with discontinuity $\mathcal{E}_{trans}$ at $\mathcal{E}_c$.

CLDM parameters:

$$\sigma_\delta = 1.38(138)\,\mathrm{MeV/fm^2}, \qquad \mathcal{C} = 0.9(1),$$

Symmetric nuclear matter and symmetry parameters:

$$n_0 = 0.16(1)\,\mathrm{fm^{-3}}, \qquad S_2 = 31(4)\,\mathrm{MeV},$$
$$e_0 = -16.0(3)\,\mathrm{MeV}, \qquad L_2 = 60(40)\,\mathrm{MeV},$$
$$K_0 = 240(40)\,\mathrm{MeV}, \qquad K_2 = 30(30)\,\mathrm{MeV},$$

Neutron matter parameters:

$$a = 13.0(3)\,\mathrm{MeV}, \qquad \alpha = 0.50(2),$$
$$b = 3.5(15)\,\mathrm{MeV}, \qquad \beta = 2.3(5),$$

Proton polaron parameters:

$$\mu_p(n_0) = -105(10)\,\mathrm{MeV}, \quad u_p = 3.1(6), \quad \frac{m_{\mathrm{eff}}}{m_p} = 0.8(1),$$

Inner-core parameters:

$$\mathcal{E}_c = 350(35)\,\mathrm{MeV}, \quad \mathcal{E}_{\max} = 0.8(4)\,\mathrm{GeV}, \quad C_{\max} = 0.8(2).$$

Table I. Parameters defining the `Central` EOS along with their uncorrelated 1σ covariance (expressed using the SI convention $3.5(15) \equiv 3.5 \pm 1.5$) used to defined the "Nuclear" error estimates prior to including information from astrophysical observations. We take the values of the CLDM parameters from the fits to the APR EOS tabulated in [40] but assign large errors to encompass missing physics such as the possibility of pasta phases. Symmetric nuclear matter and symmetry parameters have errors taken from the extensive analysis [41]. Neutron matter parameters have errors estimated from QMC calculations with various three-body interactions [15], and are consistent with recent QMC results based on chiral EFT interactions [23–25, 42]. Proton polaron parameters have errors estimated from the QMC calculations [43] and are consistent with estimates from chiral interactions [44]. The core parameters are chosen to allow for a $2M_\odot$ star at the extremes of all of our models except for the `Soft` EOS which requires a lower core transition and are given large errors to be conservative with the exception of the parameter $\mathcal{E}_c$. This is given a small error for the purposes of our statistical analysis as the dependence is highly non-linear. Variations of this parameter are considered specially in Fig. 5.

D. Parameters

Our equation of state is thus characterized by 18 parameters: σ_δ and $\mathcal{C}$, (CLDM), n_0, ε_0, K_0, (symmetric nuclear matter), S_2, L_2, K_2, (symmetry energy), a, α, b, β, (neutron matter) μ_p, u_p, m^*, (proton polaron), and $\mathcal{E}_c$, $\mathcal{E}_{\max}$, $C_{\max}$ (core). We explore various ranges of these parameters centered about the values listed in Table I, which defines our base `Central` EOS model. In addition to these central values, we repeat our analysis at a handful of different parameter values, defining the models listed in Table II. Some of these are referred to in the text, but a complete comparison is present in the supplement [20]. We now discuss how these constraints are derived from gravitational wave observations.

	Neutron Matter				Inner Core	
EOS	a [MeV]	α	b [MeV]	β	$\mathcal{E}_c$ [MeV/fm^3]	$C_{\max}$
`Central`	13.0	0.5	3.5	2.3	350	0.8
`Soft`	12.7	0.3	2	2.1		
`Stiff`	13.3	0.7	5	2.5		
`Soft_Stiff`	12.7	0.3	5	2.5		
`Stiff_Soft`	13.3	0.7	2	2.1		
`Low_`$\mathcal{E}_c$					200	
`High_`$\mathcal{E}_c$					500	
`Low_`$C_{\max}$						0.6
					$\mathcal{E}_{\mathrm{trans}}$ [MeV/fm^3]	
`Core_trans`					150	

Table II. List of changed EOS parameters compared in this work. All other parameters share the same values as the `Central` EOS in the top row, which takes the central values listed in Table I. The first four variations – `Soft`, `Stiff`, `Soft_Stiff`, and `Stiff_Soft` – refer to the properties of the neutron-matter equation of state and whether the EOS of the outer core is softer or stiffer than `Central` at low/high density. The next three variations – `Low_`$\mathcal{E}_c$, `High_`$\mathcal{E}_c$, and `Low_`$C_{\max}$ – explore variations of the core EOS. To better understand the sensitivity of our results to the properties of the core, we include one slightly different form `Core_trans` which has a first-order phase transition with discontinuity $\mathcal{E}_{\mathrm{trans}}$. (See Fig. 5.)

IV. GRAVITATIONAL WAVEFORM

Gravitational waves from merging binary neutron star systems carry information about the nuclear equations of state. During late stages of inspiral tidal interactions between neutron stars can leave imprints on the gravitational wave signal that is otherwise dominated by point-mass contributions. As mentioned earlier, tidal responses of neutron stars can be quantified by the dimensionless tidal deformability parameter $\Lambda = \frac{2}{3} k_2 c^{10} R^5/(GM)^5$, where the second Love number k_2 is weakly sensitive to the matter distribution inside the star [10]. The strong dependence of Λ on the radius R of neutron star allows us to extract information regarding nuclear EOS. Indeed, post-Newtonian (PN) theory is able to quantitatively describe the effect of the neutron star EOS on the signal by parameterizing the waveform in terms of M and Λ of component stars [10, 50].

Gravitational wave observations of inspiraling compact binaries involving neutron stars can therefore constrain Λ [3, 9]. However, since the constraint on Λ from a single BNS is weak for small to medium SNR events, multiple observations of such systems will be required for remote sources to reduce the statistical error in Ms and Λs in order to discern the effects of similar EOS [19, 51, 52]. Fortunately, tens-to-hundreds of binaries of this type [53]

are expected to be observed over the next several years by the advanced (or "second generation") LIGO.

We consider only non-spinning neutron stars here because astrophysically their spins J are expected to be small when in a BNS system; in particular it is believed that the dimensionless spin parameter $Jc/(GM^2) \leqslant 0.04$ [3, 54] We plan to study the effect of spin in a future follow up study.

The gravitational wave signal from a BNS system in a detector can be expressed as the strain

$$h(t) = A(t)e^{i\Psi(t)}, \tag{6}$$

where $A(t)$ and $\Psi(t)$ denote its amplitude and phase in the time domain. For Fisher information matrix (FIM)-based parameter estimation, we work with the Fourier transform $\tilde{h}$ of the strain above. This is constructed by adding to the point-particle part of the `TaylorF2` model at 3.5PN [55], a phase correction that is taken here to be the Fourier domain tidal waveform, with Padé fits, as prescribed in Dietrich et al. [56].

V. POPULATION MODELS

We employ different sets of stellar evolution model parameters of zero-age main sequence (ZAMS) binary stars each of which would lead to a binary neutron star system that merges within Hubble time. The differences among stellar evolution models can be large, resulting in appreciable variation in the component mass distribution. Since the tidal deformability parameter is sensitive to the masses, we explore four cases of mass distributions produced by population synthesis studies [17]. These are more realistic than the uniform or Gaussian distributions owing to the application of stellar evolution mechanism of binary stars including two important factors, namely, metallicity and the nature of the common envelop interaction in the binary.

Metallicity plays the most dominant role in determining the strength of stellar winds in main sequence stars. The larger the metallicity the larger the stellar winds, due to increased scattering cross-section of the electrons. This results in increased mass loss; therefore, the remnant mass left behind at the end of main sequence phase is reduced. This decreases the total baryonic mass content of the supernova engine at the onset of the explosion. In our study, we consider two different variants of metallicities produced by [17]. In the first case, the stellar evolution model was used with metallicity abundances being the same as solar metallicity, while in the second case 1/10th of solar metallicity was used. The latter is termed to be of sub-solar metallicity. Component masses are narrowly peaked for solar metallicity systems while subsolar metalicity system produce a wider mass distribution.

The second most important effect that can change the component masses of BNS systems is the way mass transfer takes place during the common envelop phase of stellar evolution of the binary stars. The mass transfer in the common envelop stage depends on the evolutionary phase of the two stars. In one extreme case, for example, if the common envelop phase is initiated by the star in the Hertzsprung gap stage, it is likely to transfer a significant amount of orbital angular momentum to the entire binary system. This case is denoted by "submodel A" in [17]. On the other hand, depending on the nature of interaction between the core and the envelop, one possible outcome is that during each common envelop stage for Hertzsprung gap donor stars the outer envelope acquires the significant part of the orbital angular momentum and gets ejected from the system, leaving behind the cores of the two stars to inspiral. This case is denoted by "submodel B" in [17]. Furthermore, a higher metallicity in the parent star can result in greater mass loss and consequently a less massive remnant. Therefore, we employ neutron star populations resulting from solar metallicity stars as well as those with 10% of solar metallicity. These different characteristics lead to the following four categories of population models studied here:

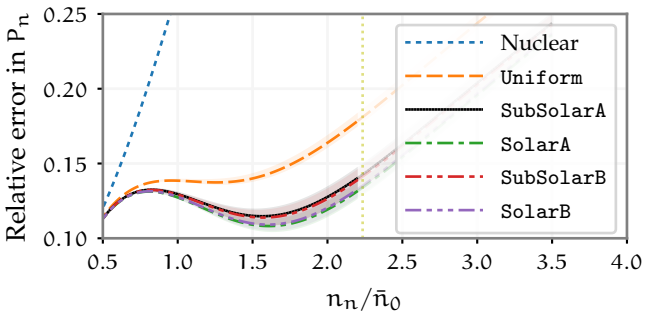

Figure 6. (color online) Population model sensitivity of the constraint on the pressure of neutron matter $P_n(n_n)$ from $N_{obs} = 15$ simulated merger events drawn from various different population models. The weaker constraints from the `Uniform` model result from distributing the events over larger mass objects. As shown in Fig. 8, this provides more information about the properties of the core at the expense of information about the lower-density regions that constrain neutron matter.

Solar metallicity submodel A (`SolarA`): These are binary neutron star populations produced by solar metallicity stars of the submodel A type.

Subsolar metallicity submodel A (`SubSolarA`): These are binary neutron star populations produced by sub-solar metallicity stars of the submodel A type.

Solar metallicity submodel B (`SolarB`): These are binary neutron star populations produced by solar metallicity stars of the submodel B type.

Subsolar metallicity submodel B (`SubSolarB`): These

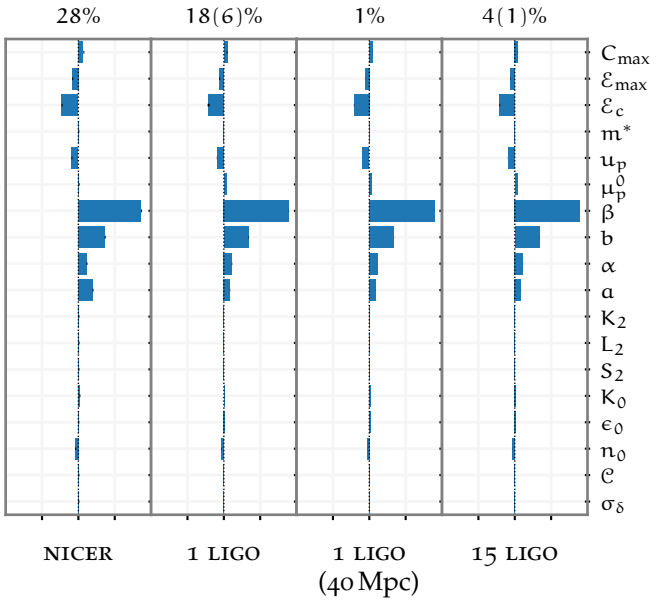

Figure 7. (color online) Principal component analysis of the simulated observational data in terms of the EOS parameters. Each column is a plot of the components of most significantly constrained eigenvector for the particular combination of observations listed at the bottom. These should be interpreted as follows: A linear combination of the log of the corresponding parameters is constrained to the tolerance shown at the top. The rightmost column shows the principal component analysis for $N_{obs} = 15$ simulated merger events drawn from the `SubSolarA` population model, and is the same as the leftmost column of Fig. 9. The 1σ errors in the tolerances, shown as small black strips in middle of the component bars, are obtained by performing 200 independent samples and demonstrate variation within the population model. *(These errors are small here, but quite visible in the second principal components of Fig. 8.)*

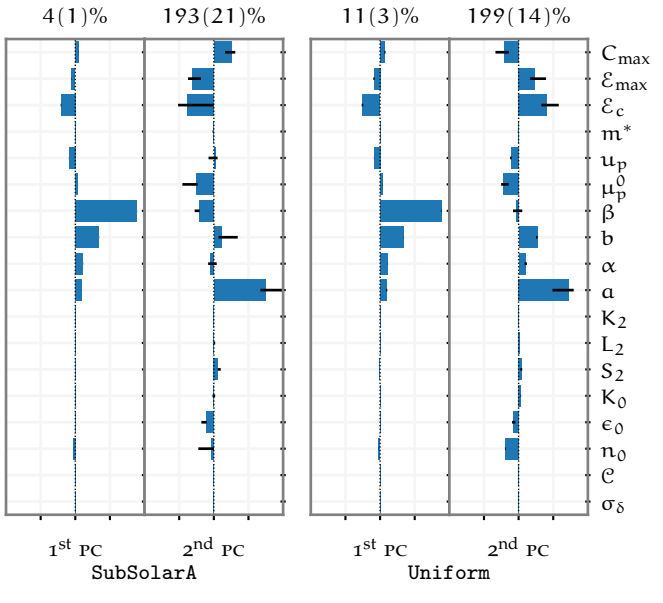

Figure 8. (color online) First two principal components for $N_{obs} = 15$ gravitational wave observations drawn from the `SubSolarA` (left) and `Uniform` (right) population models. This demonstrates the wider distribution of masses in the `Uniform` model as compared to `SubSolarA`. The narrow distribution in `SubSolarA` leads to tighter statistical constraints on the 1st principal component, but leaves other directions in parameter space poorly explored. In contrast, the `Uniform` model distributes the 15 events over a larger range of masses, reducing the constraints on the 1st principle component, but providing more information about a second direction. Even for $N_{obs} = 15$ observations, the next principal is poorly constrained at a level worse than 200%: more observations would be required to constrain this component at a useful level. Thus, neutron-star observables seem to provide tight constraints in a single direction of parameter space.

are binary neutron star populations produced by sub-solar metallicity stars of the submodel B type.

Uniform (`Uniform`): Uniform sampling of neutron stars with masses between $1.2M_\odot$ and $1.8M_\odot$.

VI. STATISTICS AND METHODS

Given a particular parameterization of the EOS, we compute the mass M, radius R, and tidal deformability parameter Λ of a neutron star with a given central density by solving the Tolman–Oppenheimer–Volkoff (TOV) equations (see e.g. [57, 58]). The signals (gravitational waveforms) from merging neutron stars is computed with the numerical relativity based frequency-domain model [56] mentioned above. From those waveforms, we compute the corresponding FIM characterizing the correlated uncertainties of the masses, M_1 and M_2, and the tidal deformabilities, Λ_1 and Λ_2 (maximizing the matched-filter over the source distance, signal time, and phase at colaescence [59]), to estimate the information obtainable in a merger event at aLIGO design sensitivity, as described below.

a. Statistical Analysis To estimate how large the noise-limited errors are of the BNS parameters ϑ, we begin by modeling the measured values after the maximum likelihood estimators (MLEs) [60]. Owing to noise, the MLE will fluctuate about the respective true values, i.e., $\hat{\vartheta} = \vartheta + \delta\vartheta$, where $\delta\vartheta$ is the random error. The extent of these fluctuations is estimated by the elements of the variance-covariance matrix, $\gamma^{ab} = \overline{\delta\vartheta^a \delta\vartheta^b}$ [60].

The matrix γ^{ab} is bounded by the signal via the Cramer-Rao inequality, which states that

$$\|\gamma\| \geqslant \|\Gamma\|^{-1} , \tag{7}$$

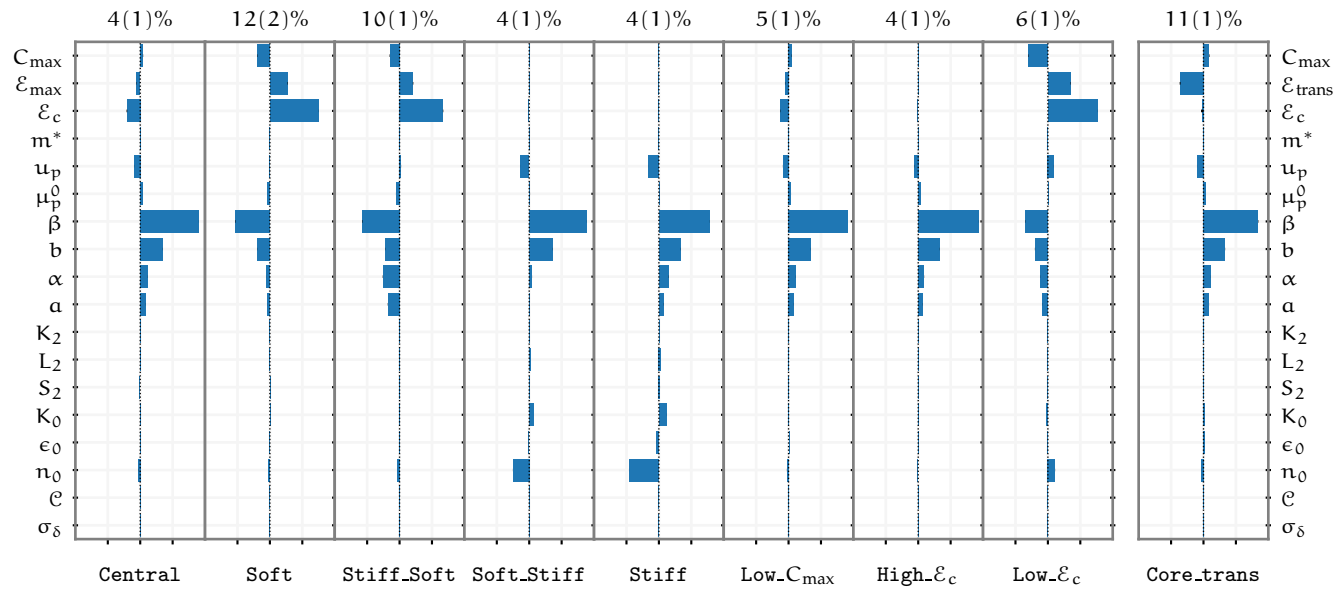

Figure 9. (color online) Principal component analysis of $N_{obs} = 15$ simulated merger events drawn from the `SubSolarA` population model for each of the EOS parameters listed in Table II. The leftmost column thus corresponds to the rightmost column of Fig. 7. This analysis makes clear the non-linear dependence of the problem on the EOS parameters: neutron star observations constrain either properties of the core for parameter values such as `Soft`, `Stiff_Soft`, `Low_`$\mathcal{E}_c$, or `Core_trans`, or the neutron matter EOS for more central values.

where Γ is the FIM:

$$\begin{aligned}\Gamma_{ab} &= \langle \partial_a \tilde{h}(\vartheta), \partial_b \tilde{h}(\vartheta) \rangle \\ &\equiv 4\Re \int df \, \frac{\partial_a \tilde{h}^*(f;\vartheta)\, \partial_b \tilde{h}(f;\vartheta)}{S_h(f)} \,. \end{aligned} \tag{8}$$

Above, ∂_a is the partial derivative with respect to the parameter ϑ^a and $S_h(f)$ is the one-sided noise power-spectral density (PSD) [60]. We take the latter to be the zero-detuned high-power PSD for aLIGO [61]. Therefore, $\Delta\vartheta^a \equiv \left(\overline{\delta\vartheta^a \, \delta\vartheta^a} \right)^{1/2} = \Gamma_{aa}^{-1/2}$ gives the lower bound on the root-mean-square (rms) error in estimating ϑ^a. The two are equal in the limit of large SNR (see, e.g., [62]). The error estimates listed here are the $\Delta\vartheta^a$ obtained from the FIM.

The FIM method is known to underestimate the error in the estimation of the masses [63]. We therefore used error-estimates for total-mass M_{tot} and mass-ratio q (i.e., the ratio of the lighter mass to heavier mass) that were obtained with Bayesian methods in Ref. [64], and set them such that the 1σ error is $\Delta M_{tot}/M_{tot} = 2\%$ and $\Delta q = 0.28$, respectively, at a single-detector SNR of 10.

The corresponding error in Λ for individual systems is consistent with that found in the available literature [19, 65, 66]. While these studies probe how accurately Λ can be measured from gravitational wave observations, they do not explore the effect of directly including inputs from nuclear theory, which is the point of this work.

To translate these correlated uncertainties in observables Ms and Λs (assuming effects of component spins to be small for $Jc/(GM^2) \leqslant 0.04$) to nuclear physics parameters, the FIM generated from the waveforms described above is transformed to the space of nuclear parameters Θ via the Jacobian $\partial\theta/\partial\Theta$ such as the partial derivative $\partial M/\partial\alpha$. These are then combined with a FIM from the base nuclear uncertainties, and information about neutron star masses and radii at levels expected of NASA's NICER mission to obtain a final covariance matrix for the 18 parameters.

The Fisher method for estimating errors has limitations, one of the main being the need for a high SNR. Bayesian methods are more reliable, but computationally much more expensive. For this latter reason use Fisher methods, whose computationally efficiency allows us to reduce source selection effects on the error estimates. We are able to quickly compute the FIM for hundreds of binaries, characterizing the variance within the population models. In spite of the drawbacks, the Fisher errors quoted here make the case to invest in Bayesian methods.

b. Methodology For a given population synthesis model, we simulate ten thousand BNS systems and distribute them uniformly in comoving volume between a luminosity distance of 100 Mpc and 400 Mpc. The latter limit is not too far from the horizon distance ($\sim$ 450 Mpc) of the network of aLIGO and Advanced Virgo detectors

beyond which BNS sources will produce signals with network SNR of less than 8. Also, below 100 Mpc we expect almost an order of magnitude fewer sources than those up to a distance of 200 Mpc. This fact notwithstanding the measurement precision for a nearby source (GW170817 was at a distance of ~40 Mpc) can rival that of a population of more distant sources. This is why we also present results for a GW170817-like source at aLIGO design sensitivity.

Our main results are summarized in Fig. 1, which shows how the constraints on the pressure of pure neutron matter $P_n(n_n)$ improve as a function of additional NICER or LIGO observations. We start from the errors listed in Table I which, for the purposes of this analysis, we interpret as uncorrelated 1σ normal errors for the parameters. In general, errors have been over-estimated to ensure that our results are conservative. The resulting FIM – a diagonal matrix of the inverse variances σ_p^{-2} – provides our starting point. From this FIM, we use forward error propagation to determine the error in pressure which we label "Nuclear".

The largest uncertainty comes from the form of the EOS in the core of the neutron star. Although a description in terms of homogeneous nuclear matter may persist to some depth, it is likely that there is some sort of phase transition to hyperonic or strange quark matter. The core EOS is thus largely unknown. To assess the impact of large variations in the core EOS, we compare the constraints obtained under a rather large variation of the core parameters, as well as in the presence of a strong first-order phase transition (`Core_trans`). This comparison was summarized in Fig. 5. Here we see rather large sensitivity to a smaller $\mathcal{E}_c$ as expected: if this is small, the core transition occurs at low density, and not enough conventional nuclear matter exists to be sensitive to gravitational wave observations. As long as the core transition is above $2n_0$ or so, the constraints on P_n are relatively insensitive to the form of the core EOS unless there is a strong first-order phase transition.

VII. CONCLUSION

The GW170817 event demonstrated that useful constraints on the neutron star structure can be obtained from gravitational waves. In this article we have addressed how future observations can provide more detailed constraints on the properties of dense matter. By separating the neutron star into four distinct regions, and providing a unique nuclear physics based parameterization of the equation of state (EOS) of the crust and outer-core, we have analyzed how measurements of the tidal deformability can constrain nuclear properties of dense matter. Our parameterization, which uses the same underlying EOS of neutron matter in both inner crust and outer core, allowed us to estimate for the first time constraints on the EOS of pure neutron matter in the density interval where controlled calculations are becoming feasible. These constraints, as they become available, will provide valuable guidance for nuclear physics. In the inner core, where the EOS is poorly constrained, the speed of sound is allowed to vary over a large range constrained only by causality and the requirement that the EOS produce a 2 solar mass neutron star. We have taken first steps to study how the large uncertainties associated with the EOS of the inner core limits our ability to constrain the EOS of neutron matter in the outer core. The results we obtain suggest that, in the absence of strong first-order transitions in the core, even a handful of detections can constrain the pressure of neutron matter in the density interval between n_0 and $2n_0$ to better than 20%.

The principal component analysis presented in Fig. 7 suggests that future LIGO observations will provide strong constraints on the density dependence of the pure neutron matter EOS in the outer core. In particular, we find that the exponent β in the neutron matter EOS defined in Eq. (2) will be well constrained. As expected, the nuclear physics parameters are better constrained when the outer core makes the dominant contribution to the tidal deformability. This is the case when the neutron matter EOS is stiff in the dense regions of the outer core and for low-mass neutron stars. If instead, the EOS in the outer core is soft or if a strong first-order phase transition were to occur at relatively low-density, constraints on the neutron matter EOS are weaker. In these cases, the inner core has a larger impact on the tidal deformability and gravitational wave detections will provide constraints for matter encountered in the inner core.

Although our focus here was to study the impact of the most common events that occur at large distances, we find that a single close by event similar to GW170817 at 40 Mpc at design sensitivity will provide valuable constraints. However, in the absence of such a nearby event, similar constraints may be realized by a dozen or so more distant events.

One limitation of our study is the simple parameterization of the EOS of the inner core. While this is adequate as a first step, to constrain the EOS of the inner core, a parameterization that allows for larger variability at high density will be needed. In addition, to gain more confidence in the constraints we have presented for neutron matter, it will be necessary to systematically marginalize over population models for neutron star masses and spins, and the uncertainty in the EOS of the inner core. A Bayesian approach would be better suited for this purpose, and we are in the processes of developing computer programs needed for such a study.

ACKNOWLEDGMENTS

We thank K. G. Arun for helpful discussions and early collaboration on waveform models with tidal corrections. We also thank Philippe Landry for carefully reading the manuscript and making useful comments. SB acknowledges partial support from the Navajbai Ratan Tata Trust. SR acknowledges support from the US Department of Energy Grant No. DE-FG02-00ER41132 and from the National Science Foundation Grant No. PHY-1430152 (JINA Center for the Evolution of the Elements). AM acknowledges partial support from the SERB Start-Up Research for Young Scientists Scheme project Grant No. SB/FTP/PS-067/2014, DST, India.

[1] J. Aasi *et al.* (LIGO Scientific), Class. Quant. Grav. **32**, 074001 (2015), arXiv:1411.4547 [gr-qc].

[2] F. Acernese *et al.* (VIRGO), Class. Quant. Grav. **32**, 024001 (2015), arXiv:1408.3978 [gr-qc].

[3] B. P. Abbott *et al.* (LIGO Scientific, Virgo), Phys. Rev. Lett. **119**, 161101 (2017), arXiv:1710.05832 [gr-qc].

[4] B. P. Abbott *et al.* (LIGO Scientific, Virgo, Fermi GBM, INTEGRAL, IceCube, AstroSat Cadmium Zinc Telluride Imager Team, IPN, Insight-Hxmt, ANTARES, Swift, AGILE Team, 1M2H Team, Dark Energy Camera GW-EM, DES, DLT40, GRAWITA, Fermi-LAT, ATCA, ASKAP, Las Cumbres Observatory Group, OzGrav, DWF (Deeper Wider Faster Program), AST3, CAASTRO, VINROUGE, MASTER, J-GEM, GROWTH, JAGWAR, CaltechNRAO, TTU-NRAO, NuSTAR, Pan-STARRS, MAXI Team, TZAC Consortium, KU, Nordic Optical Telescope, ePESSTO, GROND, Texas Tech University, SALT Group, TOROS, BOOTES, MWA, CALET, IKI-GW Follow-up, H.E.S.S., LOFAR, LWA, HAWC, Pierre Auger, ALMA, Euro VLBI Team, Pi of Sky, Chandra Team at McGill University, DFN, ATLAS Telescopes, High Time Resolution Universe Survey, RIMAS, RATIR, SKA South Africa/MeerKAT), Astrophys. J. **848**, L12 (2017), arXiv:1710.05833 [astro-ph.HE].

[5] B. P. Abbott *et al.* (LIGO Scientific, Virgo, 1M2H, Dark Energy Camera GW-E, DES, DLT40, Las Cumbres Observatory, VINROUGE, MASTER), Nature **551**, 85 (2017), arXiv:1710.05835 [astro-ph.CO].

[6] H.-Y. Chen, M. Fishbach, and D. E. Holz, Nature **562**, 545 (2018), arXiv:1712.06531 [astro-ph.CO].

[7] R. Nair, S. Bose, and T. D. Saini, Phys. Rev. **D98**, 023502 (2018), arXiv:1804.06085 [astro-ph.CO].

[8] M. Soares-Santos *et al.* (DES, LIGO Scientific, Virgo), Submitted to: Astrophys. J. (2019), arXiv:1901.01540 [astro-ph.CO].

[9] B. P. Abbott *et al.* (LIGO Scientific, Virgo), Phys. Rev. Lett. **121**, 161101 (2018), arXiv:1805.11581 [gr-qc].

[10] E. E. Flanagan and T. Hinderer, Phys. Rev. **D77**, 021502 (2008), arXiv:0709.1915 [astro-ph].

[11] S. De, D. Finstad, J. M. Lattimer, D. A. Brown, E. Berger, and C. M. Biwer, (2018), arXiv:1804.08583 [astro-ph.HE].

[12] I. Tews, J. Margueron, and S. Reddy, (2018), arXiv:1804.02783 [nucl-th].

[13] B. P. Abbott *et al.* (LIGO Scientific, Virgo), Phys. Rev. **X9**, 011001 (2019), arXiv:1805.11579 [gr-qc].

[14] I. Tews, J. Carlson, S. Gandolfi, and S. Reddy, Astrophys. J. **860**, 149 (2018), arXiv:1801.01923 [nucl-th].

[15] S. Gandolfi, A. Y. Illarionov, K. E. Schmidt, F. Pederiva, and S. Fantoni, Phys. Rev. C **79**, 054005 (2009); S. Gandolfi, A. Y. Illarionov, S. Fantoni, J. C. Miller, F. Pederiva, and K. E. Schmidt, MNRAS **404**, L35 (2010); S. Gandolfi, J. Carlson, and S. Reddy, Phys. Rev. C **85**, 032801 (2012), arXiv:1101.1921; S. Gandolfi, J. Carlson, S. Reddy, A. Steiner, and R. Wiringa, Eur. Phys. J. A **50**, 10 (2014), arXiv:1307.5815 [nucl-th].

[16] M. C. Miller and F. K. Lamb, Eur. J. Phys. A **52**, 63 (2016).

[17] M. Dominik, K. Belczynski, C. Fryer, D. Holz, E. Berti, T. Bulik, I. Mandel, and R. O'Shaughnessy, Astrophys. J. **759**, 52 (2012), arXiv:1202.4901 [astro-ph.HE].

[18] M. C. Miller, Astrophys. J. **822**, 27 (2016).

[19] M. Agathos, J. Meidam, W. Del Pozzo, T. G. F. Li, M. Tompitak, J. Veitch, S. Vitale, and C. V. D. Broeck, Phys. Rev. **D92**, 023012 (2015), arXiv:1503.05405 [gr-qc].

[20] Supplementary Material.

[21] C. J. Horowitz, Z. Ahmed, C.-M. Jen, A. Rakhman, P. A. Souder, M. M. Dalton, N. Liyanage, K. D. Paschke, K. Saenboonruang, R. Silwal, G. B. Franklin, M. Friend, B. Quinn, K. S. Kumar, D. McNulty, L. Mercado, S. Riordan, J. Wexler, R. W. Michaels, and G. M. Urciuoli, Phys. Rev. C **85**, 032501 (2012); C. Horowitz, K. Kumar, and R. Michaels, Eur. Phys. J. A **50**, 48 (2014), 10.1140/epja/i2014-14048-3; C. J. Horowitz, E. F. Brown, Y. Kim, W. G. Lynch, R. Michaels, A. Ono, J. Piekarewicz, M. B. Tsang, and H. H. Wolter, J. Phys. G **41**, 093001 (2014).

[22] K. Hebeler and A. Schwenk, Phys. Rev. C **82**, 014314 (2010); K. Hebeler, J. M. Lattimer, C. J. Pethick, and A. Schwenk, Astrophys. J. **773**, 11 (2013).

[23] G. Wlazłowski, J. W. Holt, S. Moroz, A. Bulgac, and K. J. Roche, Phys. Rev. Lett. **113**, 182503 (2014), arXiv:1403.3753.

[24] S. Gandolfi, A. Lovato, J. Carlson, and K. E. Schmidt, Phys. Rev. C **90**, 061306 (2014), arXiv:1406.3388 [nucl-th].

[25] J. E. Lynn, I. Tews, J. Carlson, S. Gandolfi, A. Gezerlis, K. E. Schmidt, and A. Schwenk, "Chiral three-nucleon interactions in light nuclei, neutron-α scattering, and neutron matter," (2015), arXiv:1509.03470.

[26] D. Page and S. Reddy, Annu. Rev. Nucl. Part. Sci. **56**, 327 (2006), arXiv:astro-ph/0608360v1.

[27] A. W. Steiner and S. Gandolfi, Phys. Rev. Lett. **108**, 081102 (2012); A. W. Steiner, J. M. Lattimer, and E. F. Brown, Astrophys. J. Lett. **765**, L5 (2013).

[28] J. M. Lattimer and A. W. Steiner, Eur. Phys. J. A **50**, 1 (2014).

[29] G. Baym, C. Pethick, and P. Sutherland, Astrophys. J. **170**, 299 (1971).

[30] J. W. Negele and D. Vautherin, Nucl. Phys. A **207**, 298 (1973).

[31] B. K. Sharma, M. Centelles, X. Vinas, M. Baldo, and G. F. Burgio, Astron. & Astrophys. **584**, A103 (2015), arXiv:1506.00375.

[32] P. Haensel, A. Y. Potekhin, and D. G. Yakovlev, *Neu-*

tron Stars 1, 1st ed., Astrophysics and Space Science Library, Vol. 326 (Springer-Verlag, New York, 2007); N. Chamel and P. Haensel, Living Rev. Relativity **11** (2008), 10.12942/lrr-2008-10, arXiv:0812.3955.
[33] A. Nelson, S. Reddy, and D. Zhou, (2018), arXiv:1803.03266 [hep-ph].
[34] J. S. Read, B. D. Lackey, B. J. Owen, and J. L. Friedman, Phys. Rev. D **79**, 124032 (2009).
[35] M. Fortin, C. Providência, A. R. Raduta, F. Gulminelli, J. L. Zdunik, P. Haensel, and M. Bejger, Phys. Rev. C **94**, 035804 (2016), arXiv:1604.01944.
[36] J. L. Zdunik, M. Fortin, and P. Haensel, "Neutron star properties and the equation of state for its core," (2016), arXiv:1611.01357.
[37] D. G. Ravenhall, C. J. Pethick, and J. R. Wilson, Phys. Rev. Lett. **50**, 2066 (1983).
[38] N. Chamel, S. Naimi, E. Khan, and J. Margueron, Phys. Rev. C **75**, 055806 (2007).
[39] J. Lattimer, C. Pethick, D. Ravenhall, and D. Lamb, Nucl. Phys. A **432**, 646 (1985).
[40] A. W. Steiner, Phys. Rev. C **85**, 055804 (2012).
[41] J. Margueron, R. Hoffmann Casali, and F. Gulminelli, Phys. Rev. C **97**, 025805 (2018).
[42] S. Gandolfi, A. Gezerlis, and J. Carlson, Annu. Rev. Nucl. Part. Sci. **65**, 303 (2015), arXiv:1501.0567.
[43] A. Roggero, A. Mukherjee, and F. Pederiva, Phys. Rev. Lett. **112**, 221103 (2014).
[44] E. Rrapaj, A. Roggero, and J. W. Holt, prc **93**, 065801 (2016).
[45] C.-H. Lee, T. T. S. Kuo, G. Q. Li, and G. E. Brown, Phys. Rev. C **57**, 3488 (1998).
[46] C. Gonzalez-Boquera, M. Centelles, X. Viñas, and A. Rios, Phys. Rev. C **96**, 065806 (2017).
[47] B.-A. Li, L.-W. Chen, and C. M. Ko, Phys. Rep. **464**, 113 (2008).
[48] A. Bulgac, M. M. Forbes, S. Jin, R. N. Perez, and N. Schunck, Phys. Rev. C **97**, 044313 (2018), arXiv:1708.08771 [nucl-th].
[49] M. Alford, Raised in discussions at the INT-16-2b program.
[50] J. Vines, E. E. Flanagan, and T. Hinderer, Phys. Rev. **D83**, 084051 (2011), arXiv:1101.1673 [gr-qc].
[51] W. Del Pozzo, T. G. F. Li, M. Agathos, C. Van Den Broeck, and S. Vitale, Physical Review Letters **111**, 071101 (2013), arXiv:1307.8338 [gr-qc].
[52] S. Bose, K. Chakravarti, L. Rezzolla, B. S. Sathyaprakash, and K. Takami, Phys. Rev. Lett. **120**, 031102 (2018), arXiv:1705.10850 [gr-qc].
[53] B. P. Abbott *et al.* (LIGO Scientific, Virgo), (2018), arXiv:1811.12907 [astro-ph.HE].
[54] K. Stovall *et al.*, Astrophys. J. **854**, L22 (2018), arXiv:1802.01707 [astro-ph.HE].
[55] A. Buonanno, B. Iyer, E. Ochsner, Y. Pan, and B. S. Sathyaprakash, Phys. Rev. **D80**, 084043 (2009), arXiv:0907.0700 [gr-qc].
[56] T. Dietrich, S. Bernuzzi, and W. Tichy, Phys. Rev. **D96**, 121501 (2017), arXiv:1706.02969 [gr-qc].
[57] T. Hinderer, Astrophys. J. **677**, 1216 (2008), arXiv:0711.2420 [astro-ph].
[58] S. Postnikov, M. Prakash, and J. M. Lattimer, Phys. Rev. D **82**, 024016 (2010), arXiv:1004.5098.
[59] P. Ajith and S. Bose, Phys. Rev. **D79**, 084032 (2009), arXiv:0901.4936 [gr-qc].
[60] C. W. Helstrom, *Elements of signal detection and estimation* (Prentice-Hall, Inc., Upper Saddle River, NJ, USA, 1995).
[61] *Advanced LIGO anticipated sensitivity curves*, Tech. Rep. LIGO-T0900288-v3 (LIGO Scientific Collaboration, https://dcc.ligo.org/LIGO-T0900288/public, 2010).
[62] M. Vallisneri, Phys. Rev. D **77**, 042001 (2008), arXiv:gr-qc/0703086.
[63] C. L. Rodriguez, B. Farr, W. M. Farr, and I. Mandel, Phys. Rev. **D88**, 084013 (2013), arXiv:1308.1397 [astro-ph.IM].
[64] C. L. Rodriguez, B. Farr, V. Raymond, W. M. Farr, T. B. Littenberg, D. Fazi, and V. Kalogera, Astrophys. J. **784**, 119 (2014), arXiv:1309.3273 [astro-ph.HE].
[65] T. Damour, A. Nagar, and L. Villain, Phys. Rev. **D85**, 123007 (2012), arXiv:1203.4352 [gr-qc].
[66] B. D. Lackey, K. Kyutoku, M. Shibata, P. R. Brady, and J. L. Friedman, Phys. Rev. **D85**, 044061 (2012), arXiv:1109.3402 [astro-ph.HE].

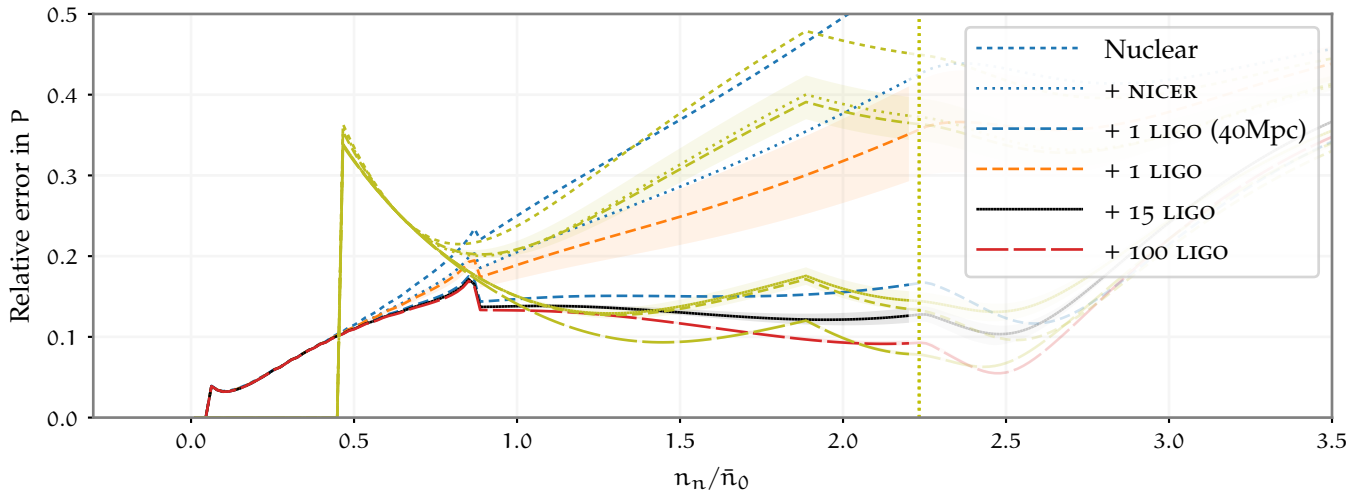

Figure 10. (color online) Relative constraints on the pressure P of nuclear matter in β-equilibrium for the `Central` EOS (dark curves) and a polytropic EOS (light curves) with the same form as [34] with parameters fit to give a similar mass-radius curve, but using the same core EOS as ours. (Note: Kinks in these curves occur when the form of the EOS changes - for example, just below $n = 2n_0$, the from of the polytrope [34] changes.)

Appendix A: Supplementary Material

1. Surface Term in the CLDM

In our implementation of the CLDM, we use the following surface term with an effective surface tension $\sigma(n_n^i, n_p^i) = \sigma_0/(1 - C_{sym} f(x_p)) \approx \sigma_0(1 - C_{sym}\beta^2 + \mathcal{O}(\beta^4))$ following [39] (see also [40]):

$$E = 4\pi r_p^2 \, \sigma_0 \frac{1}{1 - \frac{C_{sym}}{96}\left(16 - x_p^{-3} - (1-x_p)^{-3}\right)} \tag{A1a}$$

$$= 4\pi r_p^2 \, \sigma_0 \left(1 - C_{sym}\beta^2 + \mathcal{O}(\beta^4)\right), \tag{A1b}$$

where $x_p = n_p^i/(n_p^i + n_n^i)$ is the proton fraction in the nucleus, and $\beta = (n_n^i - n_p^i)/(n_p^i + n_n^i) = 1 - 2x_p$. We parameterize this as $C_{sym} = \sigma_\delta/\sigma_0$ where $\sigma_\delta \approx 1.38\,\mathrm{MeV/fm^2}$ is held fixed as a parameter of the theory, and σ_0 is varied to smoothly match the tabulated outer-crust data.

2. Polytropes

In Fig. 10 we compare the constraints obtained on the total pressure $P(n_B)$ of nuclear matter in β-equilibrium using our `Central` unified parameterization with those obtained using the piecewise polytropic EOS in [34]. To better compare these, we do the following:

1. Fit the parameters of the polytrope to best match our `Central` EOS: $\log(p_1) = 34.3$, $\Gamma_1 = 2.60$, $\Gamma_2 = 3.81$, and $\Gamma_3 = 2.91$.
2. We use the same speed-of-sound core parameterization with $E_c = 350.0\,\mathrm{MeV/fm^3}$, $E_{max} = 800.0\,\mathrm{MeV/fm^3}$, $C_{max} = 0.8$ as our `Central` EOS.
3. We start with a bare "Nuclear" constraint by computing the 1.2σ covariance matrix of the parameters from Table III of [34] over the following EOS models that have a small pressure $P(n_0) < 3\,\mathrm{MeV/fm^3}$ at saturation density: PAL6, SLy, APR1, APR2, APR3, APR4, FPS, WFF1, WFF2, WFF3, BBB2, BPAL12, ENG, MPA1, BGN1H1, PCL2, ALF1, ALF2, ALF3, and ALF4. (This excludes some models with hyperon (GNH3, H1-7), pion (PS), and kaon (GS1-2) condensates, as well as the strange-quark matter models MS1-2, which all have significantly higher saturation pressures $P(n_0) > 3\,\mathrm{MeV/fm^3}$). This gives similar bare "Nuclear" errors as our `Central` model at and above saturation density.

We note that the constraints on P are very similar to those from our "Nuclear" parameter set. To obtain this, however, it was critical to use correlated errors in the polytrope parameters. To this end, taking a polytropic EOS with uncorrelated priors is inadvisable. Only once correlated priors are used does the polytropic equation of state provide constraints comparable to those that can be obtained from our nuclear parameterization.

3. Tabulated EoS Data

Here we present somewhat tighter constraints on tabulated EOS data, required to ensure convexity, than we have seen presented in the literature. Suppose we have

an interval with tabulated density, pressure, and energy $n_{0,1}$, $P_{0,1}$, and $\mathcal{E}_{0,1}$. If these data come from an equation of state that satisfies thermodynamic convexity $\mathcal{E}''(n) = P'(n)/n \geqslant 0$ and causality $\mathcal{E}'(P) \geqslant 1$, then each interval must satisfy the following conditions:

$$P_1 - P_0 \leqslant \mathcal{E}_1 - \mathcal{E}_0, \qquad \frac{\mathcal{E}_1 + P_1}{\sqrt{(\mathcal{E}_0 + P_0)(E_0 + 2P_1 - P_0)}} \leqslant \frac{n_1}{n_0} \leqslant \frac{\sqrt{(\mathcal{E}_1 + P_1)(\mathcal{E}_1 + 2P_0 - P_1)}}{\mathcal{E}_0 + P_0}. \tag{A2}$$

The tabulated date in [31] used for the outer crust required some minor corrections to ensure these constraints are met.

4. Thermodynamic Relationships

Here we briefly review some $T = 0$ thermodynamic relationships for an EOS with a single conserved component with density n and chemical potential μ, energy density $\mathcal{E}$, energy per particle E, and pressure P. These are used at various places throughout the text, such as relating the slope of the symmetry energy $L = 3P_n(n_0)/n_0$ to the pressure of neutron matter in Eq. (1b)

$$E(n) = \frac{\mathcal{E}(n)}{n}, \qquad \mu = \mathcal{E}'(n), \tag{A3a}$$

$$P = \mu n - \mathcal{E} = n^2 E'(n), \tag{A3b}$$

$$C = \frac{c_s^2}{c^2} = \frac{dP}{d\mathcal{E}} = \frac{P'(n)}{\mathcal{E}'(n)} = \frac{n\mu'(n)}{\mu}. \tag{A3c}$$

5. Comparison Plots

On the following pages, we provide comparison plots for all of the EOS models discussed in the text.

Central

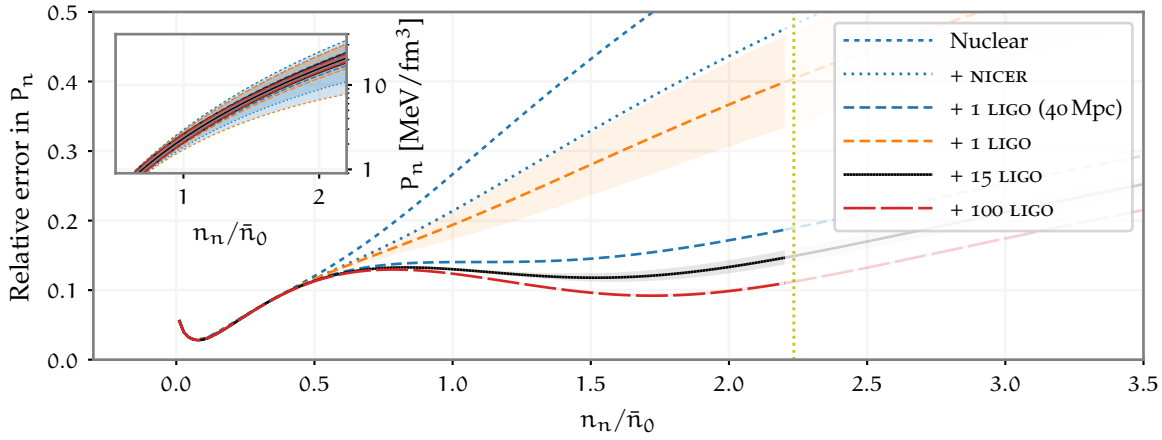
Relative error in P_n
$n_n/\bar{n}_0$
P_n [MeV/fm^3]
Nuclear
+ NICER
+ 1 LIGO (40 Mpc)
+ 1 LIGO
+ 15 LIGO
+ 100 LIGO

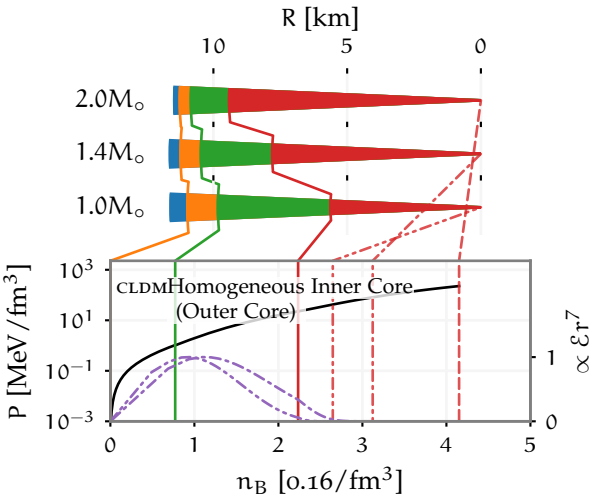
R [km]
2.0$M_\odot$
1.4$M_\odot$
1.0$M_\odot$
P [MeV/fm^3]
CLDM
Homogeneous Inner Core
(Outer Core)
$\propto \varepsilon r^7$
n_B [0.16/fm^3]

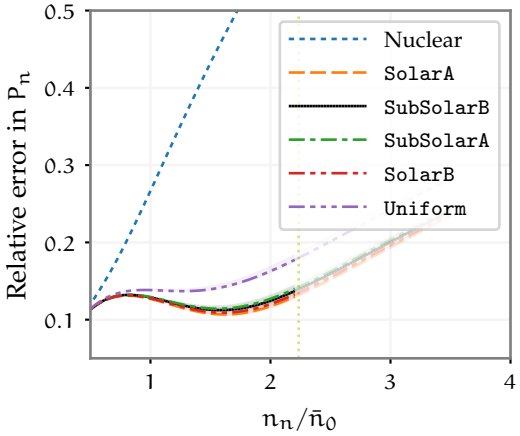
Relative error in P_n
$n_n/\bar{n}_0$
Nuclear
SolarA
SubSolarB
SubSolarA
SolarB
Uniform

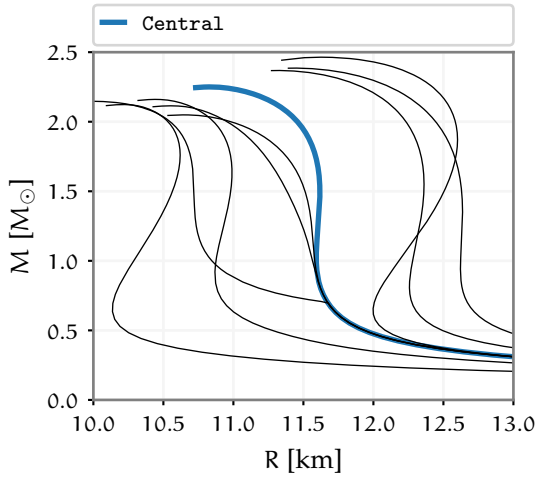
Central
M [$M_\odot$]
R [km]

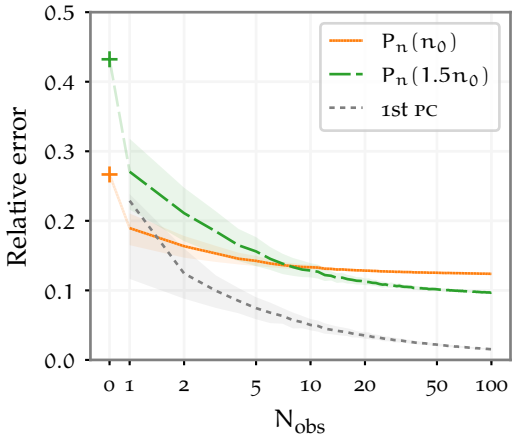
Relative error
$P_n(n_0)$
$P_n(1.5n_0)$
1st PC
N_{obs}

Soft

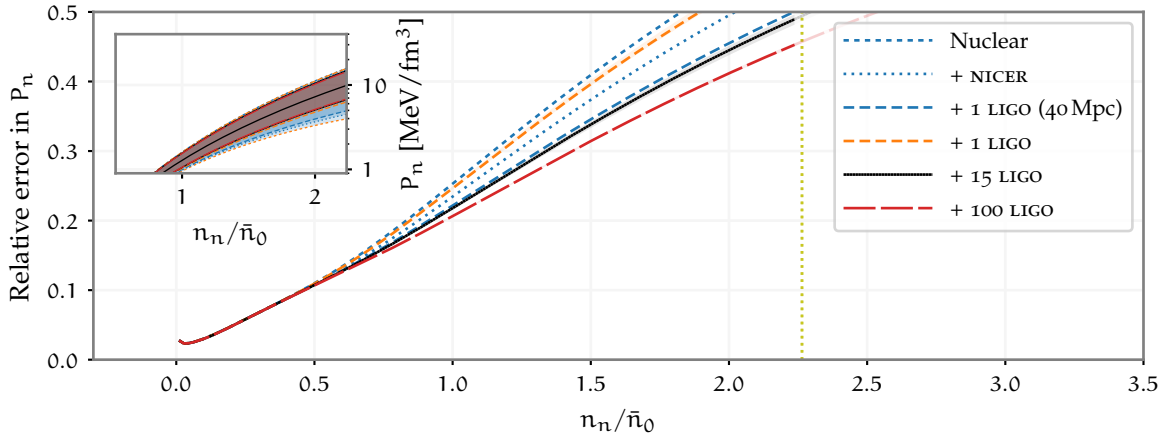
Relative error in P_n
P_n [MeV/fm^3]
$n_n/\bar{n}_0$
Nuclear
+ NICER
+ 1 LIGO (40 Mpc)
+ 1 LIGO
+ 15 LIGO
+ 100 LIGO

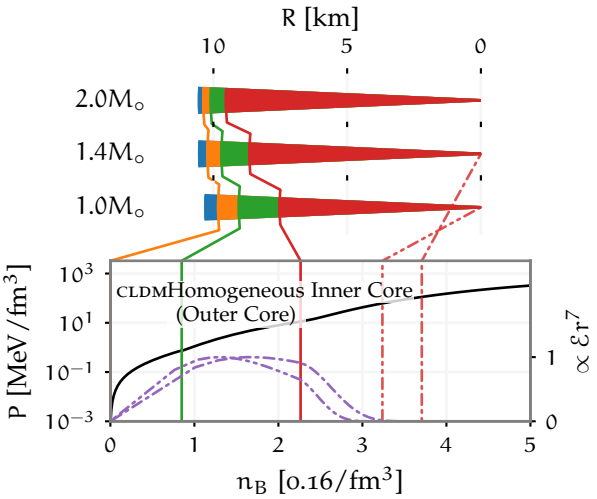
R [km]
2.0$M_\odot$
1.4$M_\odot$
1.0$M_\odot$
P [MeV/fm^3]
CLDM
Homogeneous Inner Core
(Outer Core)
$\propto \varepsilon r^7$
n_B [0.16/fm^3]

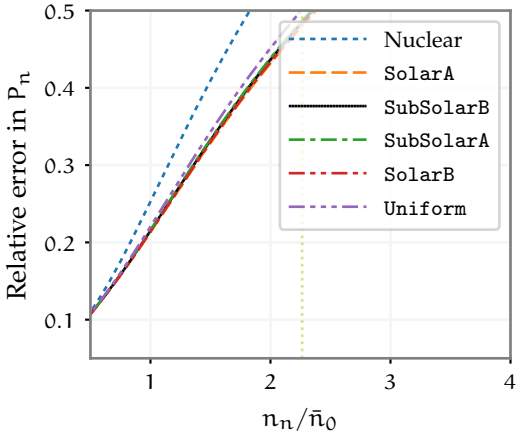
Relative error in P_n
$n_n/\bar{n}_0$
Nuclear
SolarA
SubSolarB
SubSolarA
SolarB
Uniform

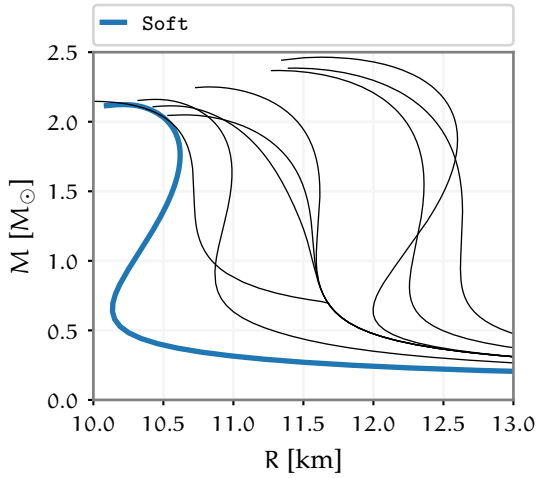
Soft
M [$M_\odot$]
R [km]

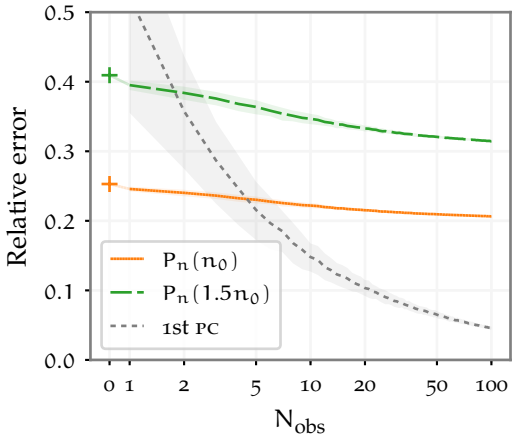
Relative error
$P_n(n_0)$
$P_n(1.5n_0)$
1st PC
N_{obs}

Stiff_Soft

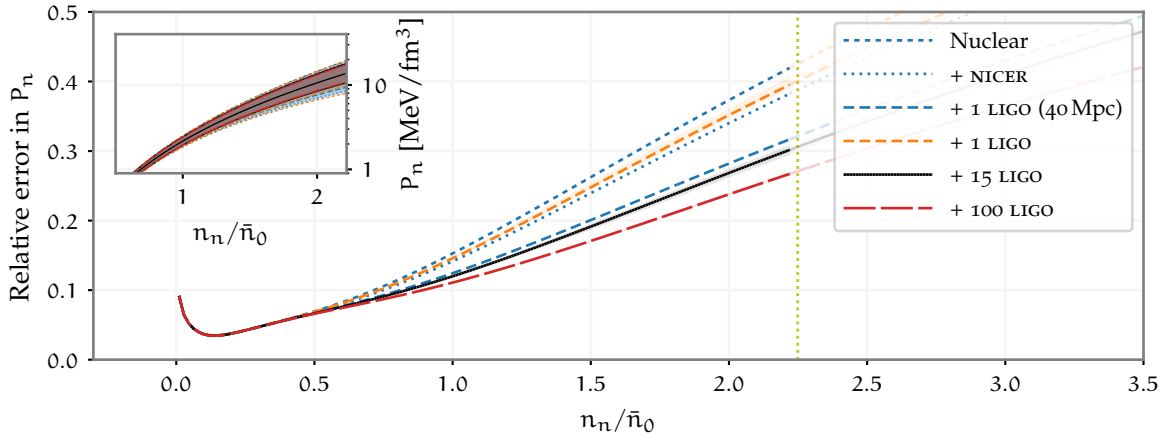
Relative error in P_n
P_n [MeV/fm^3]
$n_n/\bar{n}_0$
Nuclear
+ NICER
+ 1 LIGO (40 Mpc)
+ 1 LIGO
+ 15 LIGO
+ 100 LIGO

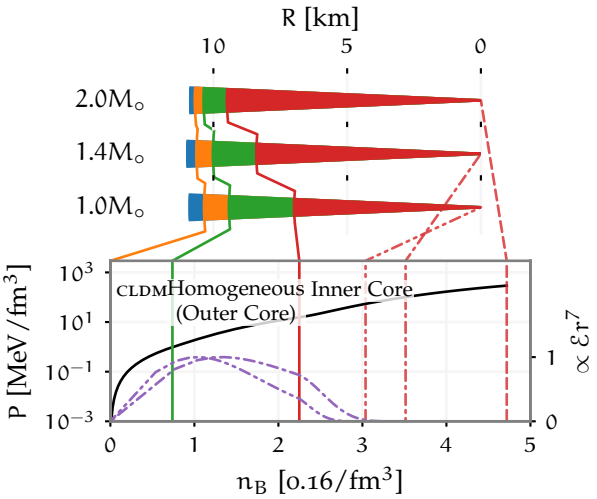
R [km]
2.0$M_\odot$
1.4$M_\odot$
1.0$M_\odot$
P [MeV/fm^3]
CLDM
Homogeneous Inner Core
(Outer Core)
$\propto \varepsilon r^7$
n_B [0.16/fm^3]

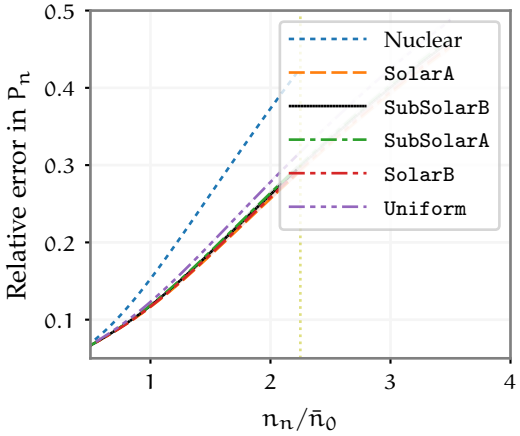
Relative error in P_n
Nuclear
SolarA
SubSolarB
SubSolarA
SolarB
Uniform
$n_n/\bar{n}_0$

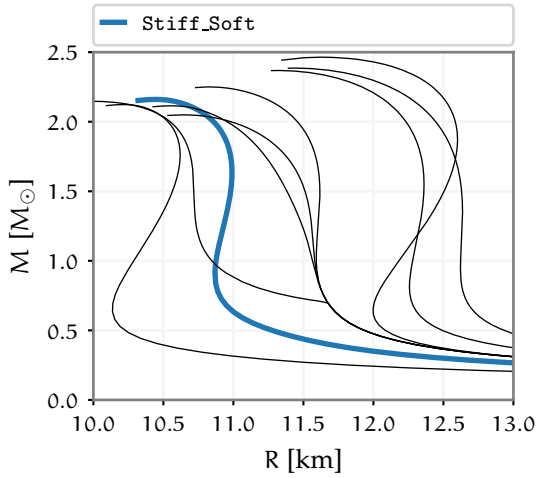
Stiff_Soft
M [$M_\odot$]
R [km]

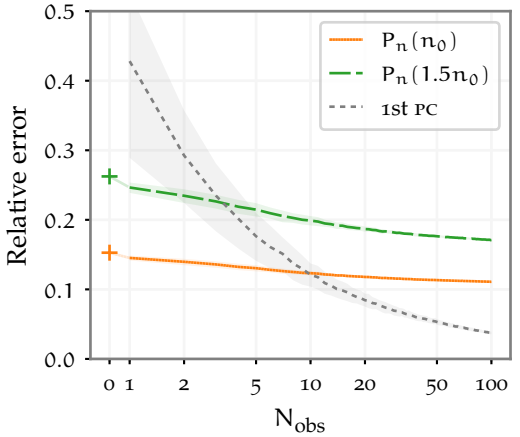
Relative error
$P_n(n_0)$
$P_n(1.5n_0)$
1st PC
N_{obs}

Soft_Stiff

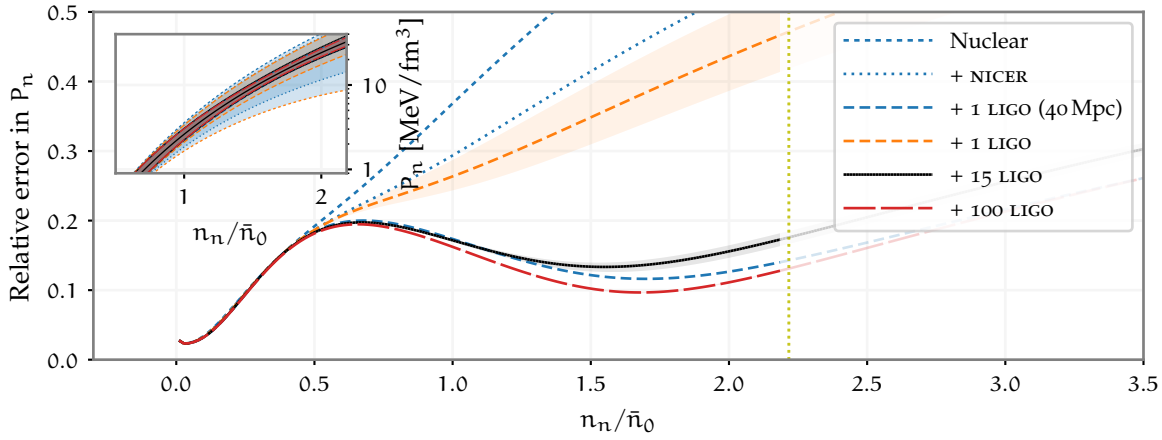
Relative error in P_n
P_n [MeV/fm^3]
$n_n/\bar{n}_0$
Nuclear
+ NICER
+ 1 LIGO (40 Mpc)
+ 1 LIGO
+ 15 LIGO
+ 100 LIGO

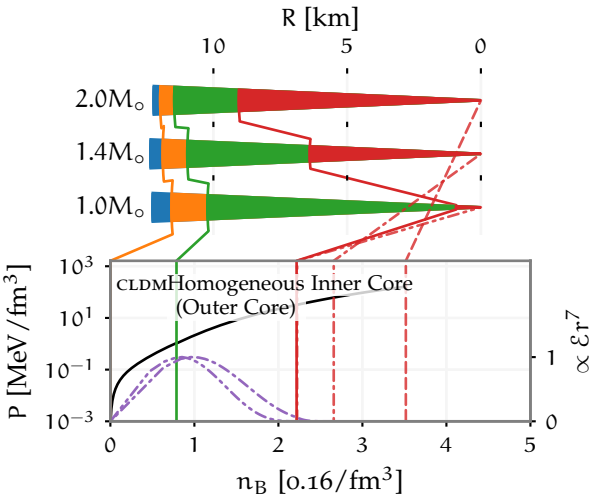
R [km]
2.0$M_\odot$
1.4$M_\odot$
1.0$M_\odot$
P [MeV/fm^3]
CLDM
Homogeneous Inner Core
(Outer Core)
$\propto \varepsilon r^7$
n_B [0.16/fm^3]

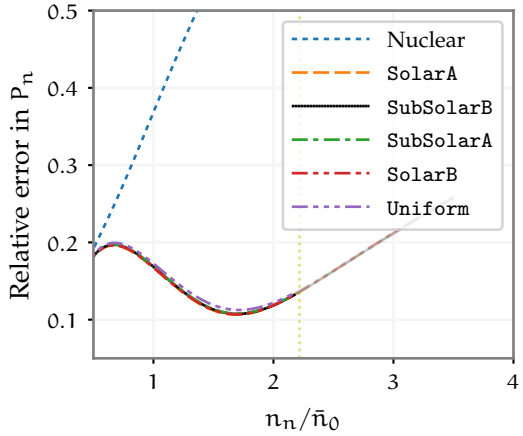
Relative error in P_n
Nuclear
SolarA
SubSolarB
SubSolarA
SolarB
Uniform
$n_n/\bar{n}_0$

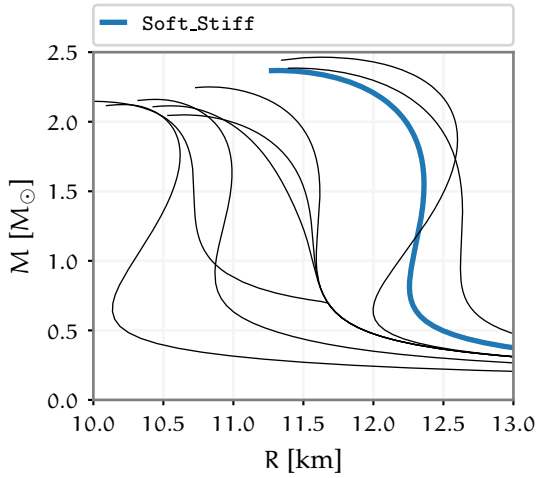
Soft_Stiff
M [$M_\odot$]
R [km]

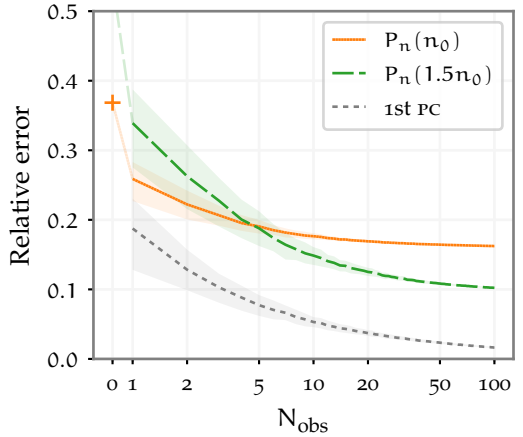
Relative error
$P_n(n_0)$
$P_n(1.5n_0)$
1st PC
N_{obs}

Stiff

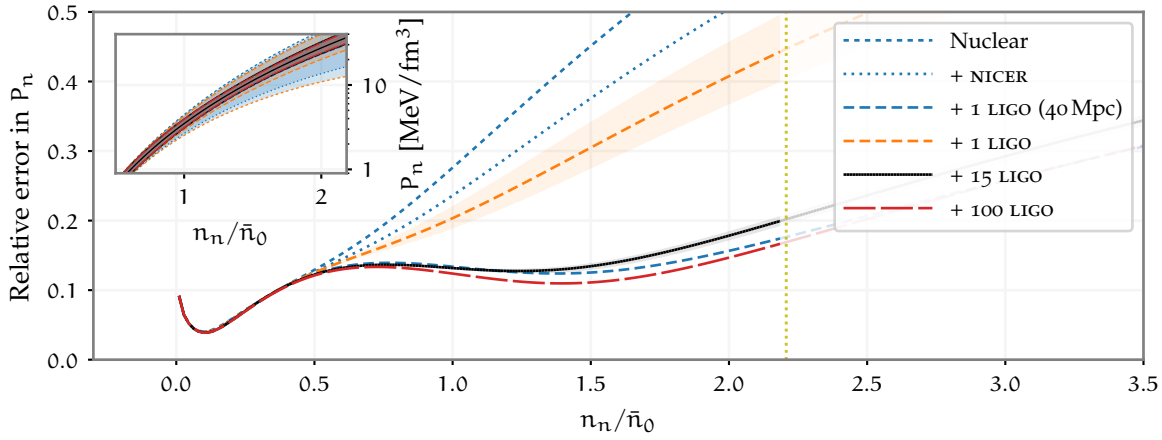
Relative error in P_n
P_n [MeV/fm^3]
$n_n/\bar{n}_0$
Nuclear
+ NICER
+ 1 LIGO (40 Mpc)
+ 1 LIGO
+ 15 LIGO
+ 100 LIGO

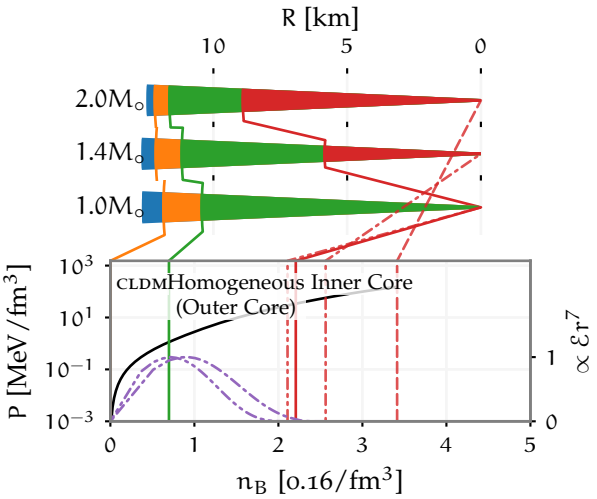
R [km]
2.0$M_\odot$
1.4$M_\odot$
1.0$M_\odot$
P [MeV/fm^3]
CLDM
Homogeneous Inner Core
(Outer Core)
$\propto \varepsilon r^7$
n_B [0.16/fm^3]

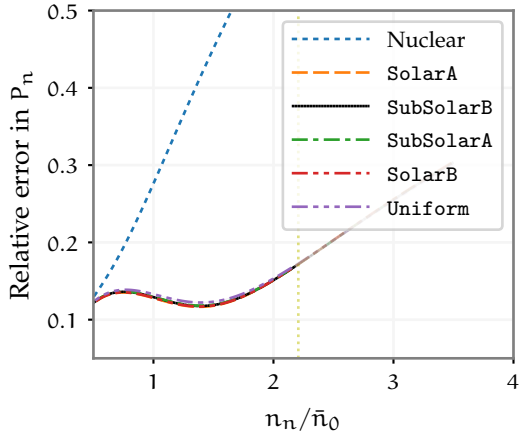
Relative error in P_n
$n_n/\bar{n}_0$
Nuclear
SolarA
SubSolarB
SubSolarA
SolarB
Uniform

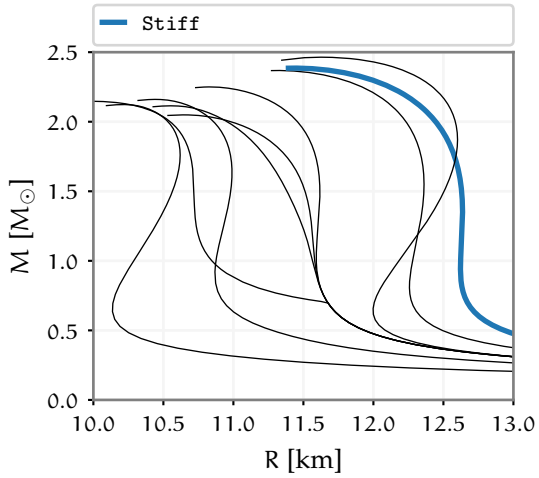
Stiff
M [$M_\odot$]
R [km]

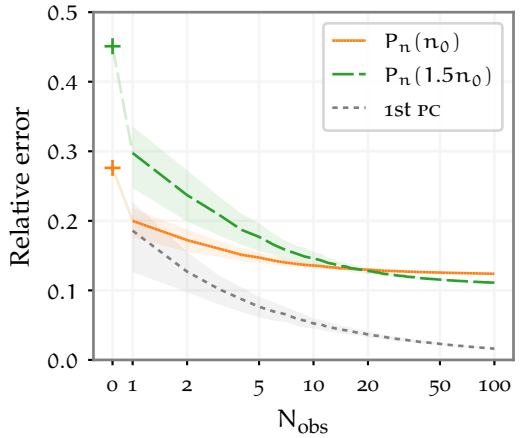
Relative error
N_{obs}
$P_n(n_0)$
$P_n(1.5n_0)$
1st PC

Low_C_{max}

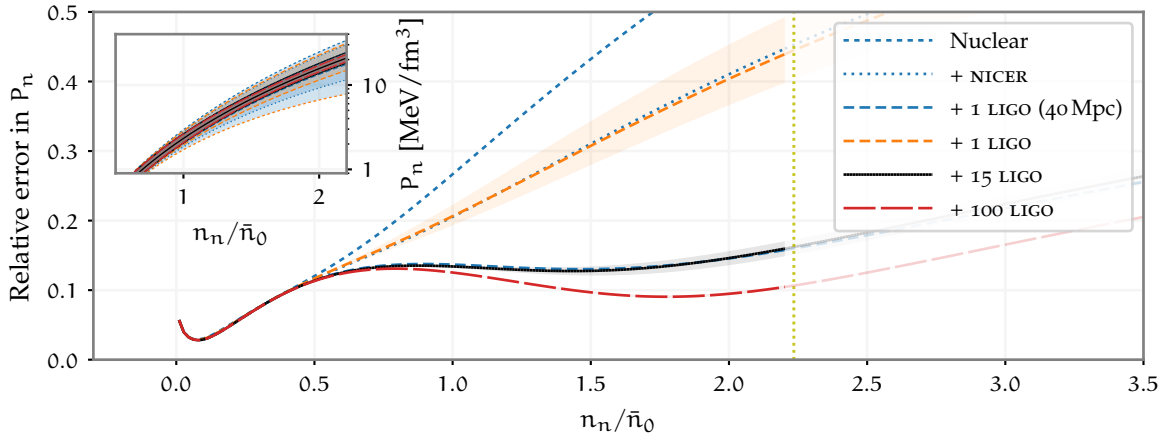
Relative error in P_n
P_n [MeV/fm^3]
$n_n/\bar{n}_0$
Nuclear
+ NICER
+ 1 LIGO (40 Mpc)
+ 1 LIGO
+ 15 LIGO
+ 100 LIGO

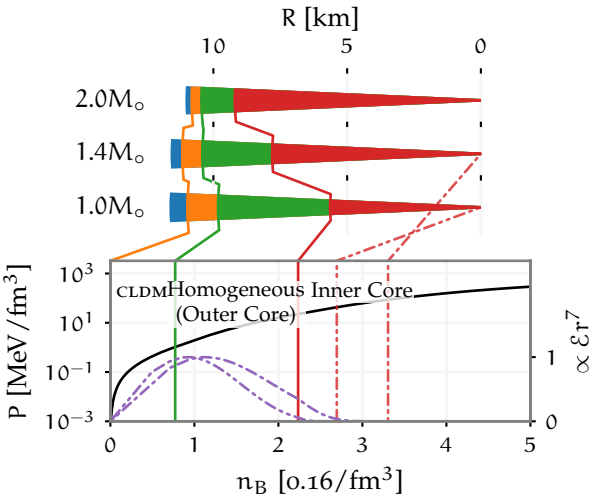
R [km]
2.0$M_\odot$
1.4$M_\odot$
1.0$M_\odot$
P [MeV/fm^3]
CLDM
Homogeneous Inner Core
(Outer Core)
$\propto \varepsilon r^7$
n_B [0.16/fm^3]

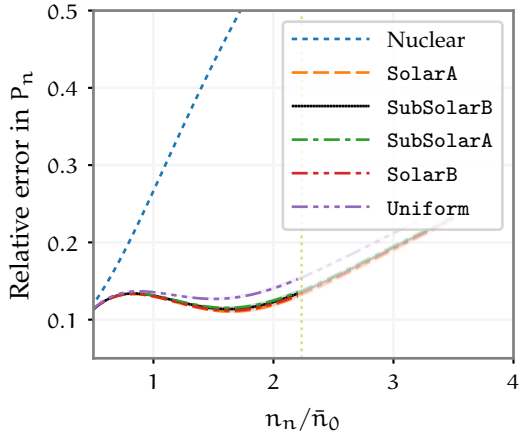
Relative error in P_n
$n_n/\bar{n}_0$
Nuclear
SolarA
SubSolarB
SubSolarA
SolarB
Uniform

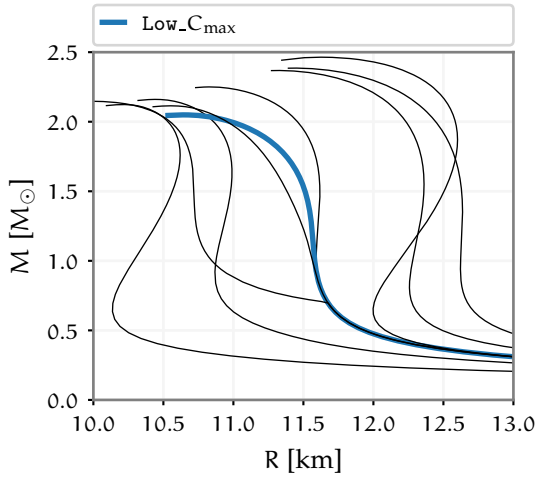
Low_C_{max}
M [$M_\odot$]
R [km]

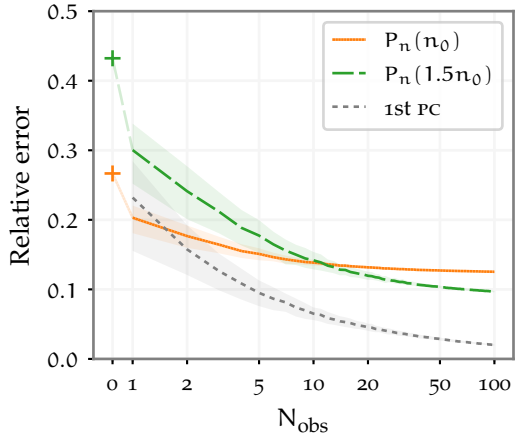
Relative error
$P_n(n_0)$
$P_n(1.5n_0)$
1st PC
N_{obs}

High_$\mathcal{E}_c$

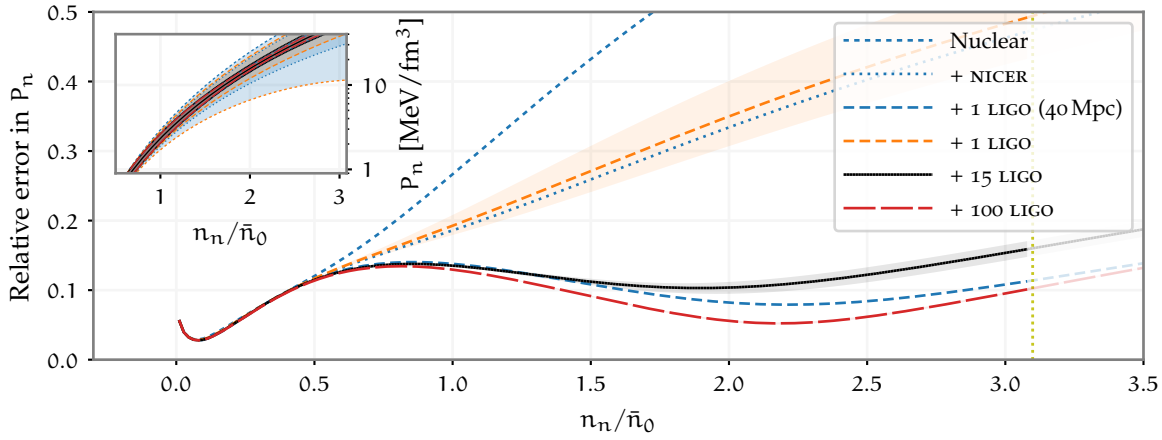

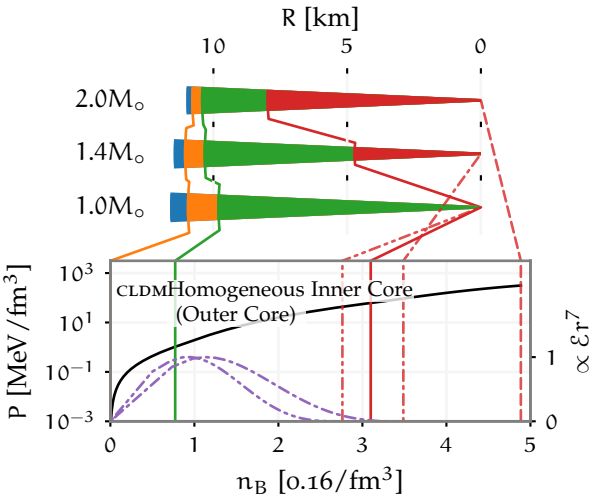

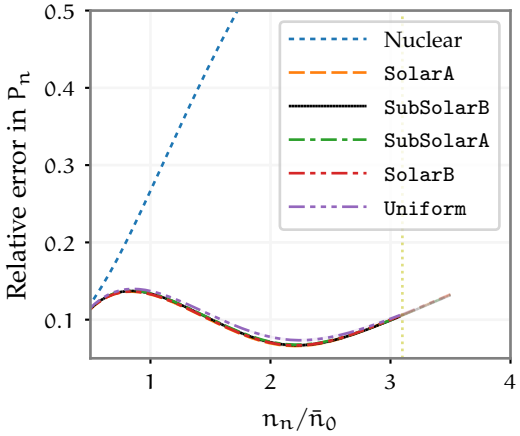

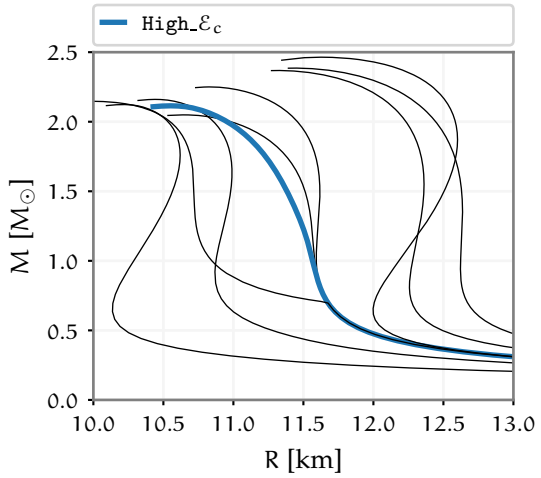

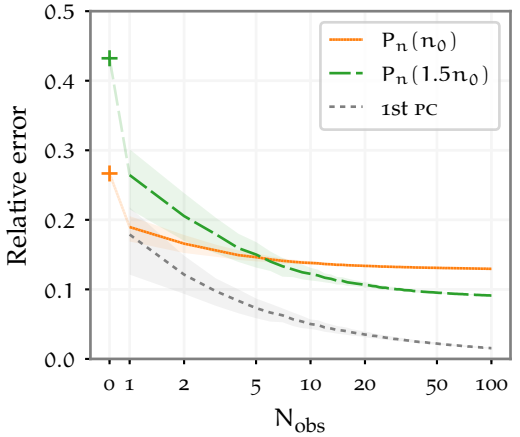

Low_$\mathcal{E}_c$

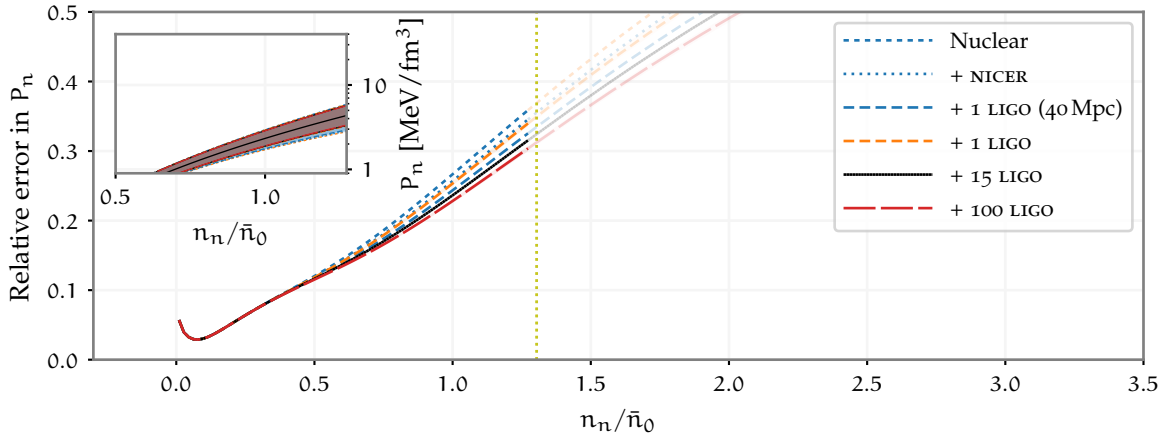

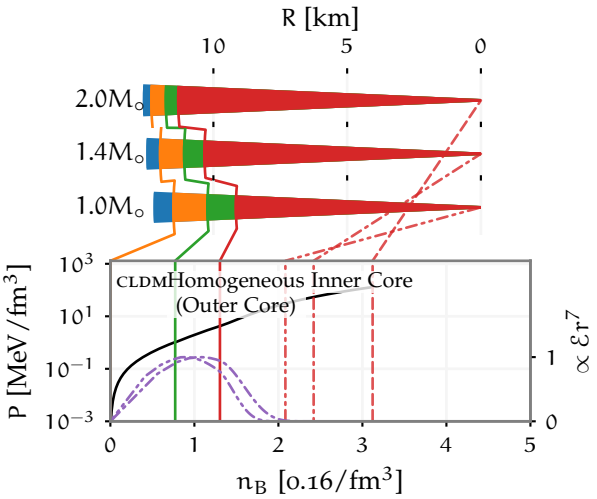

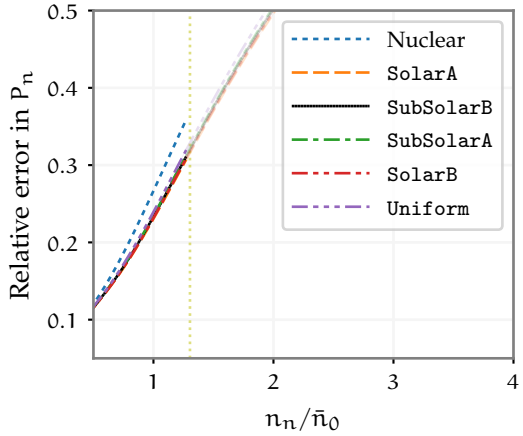

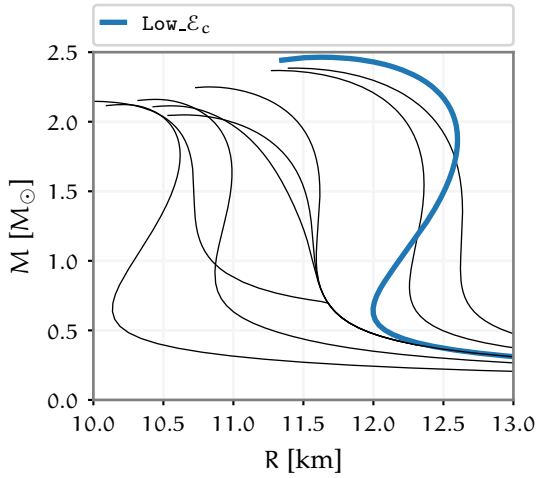

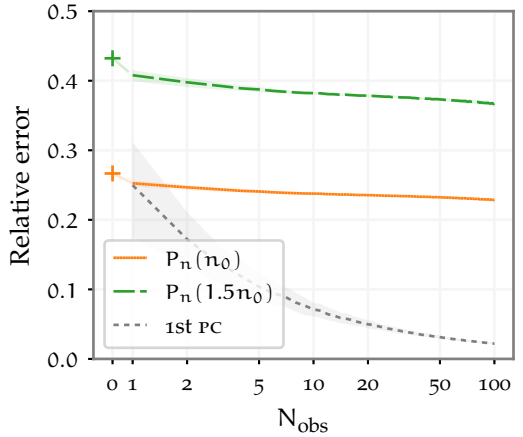

Core_trans

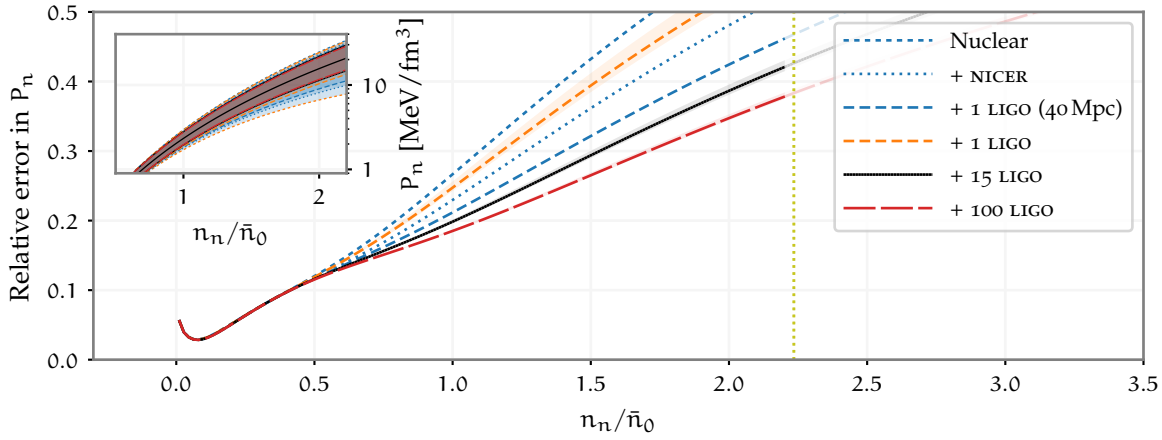
Relative error in P_n
P_n [MeV/fm^3]
$n_n/\bar{n}_0$
Nuclear
+ NICER
+ 1 LIGO (40 Mpc)
+ 1 LIGO
+ 15 LIGO
+ 100 LIGO

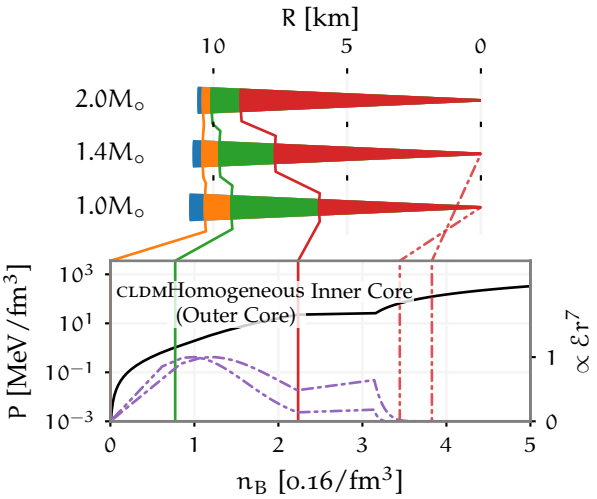
R [km]
2.0$M_\odot$
1.4$M_\odot$
1.0$M_\odot$
P [MeV/fm^3]
CLDMHomogeneous Inner Core
(Outer Core)
$\propto \varepsilon r^7$
n_B [0.16/fm^3]

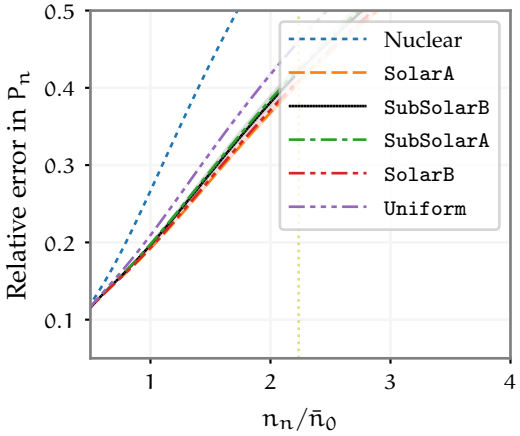
Relative error in P_n
$n_n/\bar{n}_0$
Nuclear
SolarA
SubSolarB
SubSolarA
SolarB
Uniform

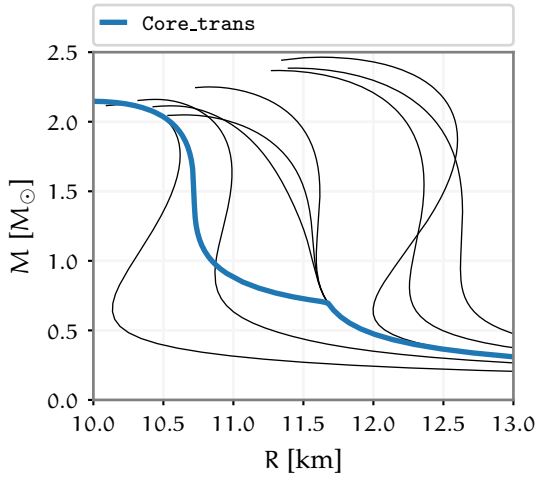
Core_trans
M [$M_\odot$]
R [km]

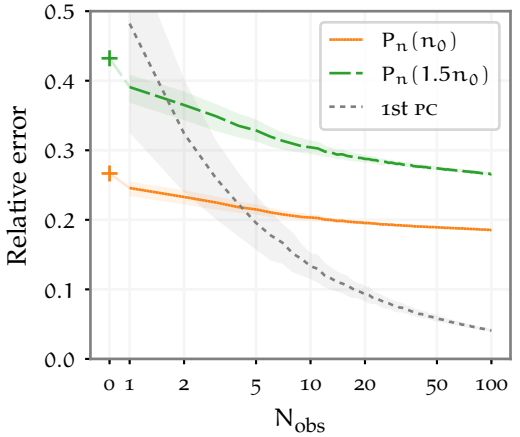
Relative error
N_{obs}
$P_n(n_0)$
$P_n(1.5n_0)$
1st PC